HAL
open science

On-chip tunneling spectroscopy of colloidal quantum dots

Hongyue Wang

To cite this version:

Hongyue Wang. On-chip tunneling spectroscopy of colloidal quantum dots. Chemical Physics [physics.chem-ph]. Université Pierre et Marie Curie - Paris VI, 2015. English. NNT : 2015PA066555 . tel-01327979

HAL Id: tel-01327979

https://theses.hal.science/tel-01327979v1

Submitted on 7 Jun 2016

HAL is a multi-disciplinary open access archive for the deposit and dissemination of scientific research documents, whether they are published or not. The documents may come from teaching and research institutions in France or abroad, or from public or private research centers.

L'archive ouverte pluridisciplinaire **HAL**, est destinée au dépôt et à la diffusion de documents scientifiques de niveau recherche, publiés ou non, émanant des établissements d'enseignement et de recherche français ou étrangers, des laboratoires publics ou privés.

Université Pierre et Marie Curie

Ecole doctorale Physique et Chimie des Matériaux (ED 397)

Laboratoire Physique et Etude des Matériaux (CNRS-UMR8213)

On-chip Tunneling Spectroscopy of Colloidal Quantum Dots

Hongyue WANG

Thèse de doctorat de Physique et Chimie des Matériaux

Présentée et soutenue publiquement le 24 Novembre 2015

Devant un jury composé de :

Shukla Abhay, IMPMC, UPMC, Président du jury
Grandidier Bruno, CNRS, Université Lille, Rapporteur
Lafarge Philippe, Laboratoire MPQ, Université Paris 7, Rapporteur
Respaud Marc, LPCNO, INSA, Toulouse, Examinateur
Aubin Hervé, LPEM, ESPCI, Directeur de Thèse

Acknowledgements

First of all, I would like to thank the group leader, Hervé Aubin, who is my advisor and give me the opportunity to be a member of this research group. I am thankful for your patience, support, enthusiasm and your wide knowledge.

I would like to thank our group members, Alexandre Zimmers, Qian Yu, Alireza Mottaghizadeh, Alexandre Assouline and Tianzhen Zhang, my thesis work would never had succeeded without their helps.

I would like to thank the professors, researchers and engineers at LPEM, Benoit Dubertret, Emmanuel Lhuillier, Jérôme Lesueur, Ricardo Lobo, Kamran Behnia, Benoit Fauqué, Zhuoying Chen, Xiangzhen Xu and Armel Descamps-Mandine. I am also thankful to LPEM administrative staff, Sophie, Marie-Claude, Josiane and Francis.

I would like to thank my family and my friends for their helps and support.

Abstract

In this manuscript, I will describe my thesis work on the fabrication and measurement of single Quantum Dot (QD) tunnel junctions. After the introduction chapter, the second chapter of this thesis will introduce the fundamental concepts needed to describe a single QD junction, such as the concepts of quantum confinement and Coulomb blockade. Furthermore, I will describe the most emblematic QD systems. In the third chapter of this manuscript, I will describe the ligands exchange methods, the sample fabrication methods and the measurement setups. In the fourth chapter, I will describe my tunneling spectroscopy study of single PbS QDs as function of temperature and gate voltage. Three distinct signatures of strong electron-phonon coupling are observed in the Electron Tunneling Spectrum (ETS) of these QDs. In the shell-filling regime, the 8 times degeneracy of the electronic levels is lifted by the Coulomb interactions and allows the observation of phonon sub-bands that result from the emission of optical phonons. At low bias, a gap is observed in the spectrum that cannot be closed with the gate voltage, which is a distinguishing feature of the Franck-Condon blockade. From the data, a Huang-Rhys factor in the range $S \sim 1.7 - 2.5$ is obtained. Finally, in the shell tunneling regime, the optical phonons appear in the inelastic ETS

d^2I/dV^2. In the fifth chapter, I present a tunnel spectroscopy study of single HgSe QDs as function of gate voltage and light illumination. Upon tuning the gate voltage, different occupation levels of the QD can be reached. The gap observed in the ETS changes with the occupation level. A large inter-band gap, about 0.9 eV, is observed for the empty QDs, and an intra-band gap about 0.2 eV is observed for the doubly occupied QD. Upon illuminating the QD junction, a photocurrent can be measured using an especially designed demodulation technique. From this measurement, the lifetime $\tau \sim 65\ \mu s$ is extracted for the photogenerated electron-hole in the QD.

Contents

Contents **iv**

1 Introduction **1**

2 State of the art **5**

2.1 Basic concepts 5

2.1.1 Quantum tunneling 5

2.1.2 Coulomb blockade 12

2.1.3 Tunneling spectroscopy 15

2.2 Band structure of semiconducting QDs 17

2.2.1 Density of states 17

2.2.2 Band structure of PbS QDs 19

2.2.3 Band structure of HgSe QDs 21

2.3 Examples of tunnel spectroscopy in different QD systems 23

2.3.1 Microfabricated large QDs 25

2.3.2 Nanotubes and nanowires based QDs 27

2.3.3 STM spectroscopy of colloidal semiconducting QDs 29

2.3.4 On-chip spectroscopy of colloidal semiconducting QDs . . 30

2.3.5 Colloidal metallic nanocrystals 32
2.3.6 Conclusion 35

3 Samples preparation and experimental setups 38

3.1 Samples preparation 38
3.1.1 Synthesis of PbS QDs 38
3.1.2 Synthesis of HgSe QDs 39
3.1.3 Ligands exchange 41
3.1.4 Fabrication of nanogaps circuits 42
3.2 Experimental setups 44
3.2.1 The projection system 45
3.2.2 Measurement methods 46
3.2.3 The electrospray ionization system 51
3.2.4 Cryostat measurement setup 54

4 Tunneling spectroscopy of single PbS QDs 58

4.1 Coulomb blockade in single PbS QDs 61
4.2 Phonon sub-bands and Frank-Condon blockade 68
4.2.1 Phonon sub-bands in electron tunneling spectrum 68
4.2.2 Frank-Condon blockade 69
4.3 Inelastic tunneling spectroscopy of PbS QDs 73
4.4 Capacitive coupling between the gate and QDs 74
4.5 Conclusion 77

5 Tunneling spectroscopy of single HgSe QDs 78

5.1 The interband and intraband transition of HgSe QD 80

5.2 Photocurrent measurement on a single HgSe QD 84
5.3 Conclusion 88

6 Conclusions and prospects **89**

7 Publications **92**

. 92

References **93**

Chapter 1 93
Chapter 2 95
Chapter 3 98
Chapter 4 100
Chapter 5 102

Chapter 1

Introduction

Nanostructured materials may be defined as those materials whose structural elements—clusters, crystallites or molecules—have dimensions in the 1 to 100 nm range[1]. The investigation of nanostructured materials attracted much attention and many results were obtained on Quantum Dots (QDs)[2–4], nano-wires[5, 6] and nano-plates[7–9]. The possibility of controlling the size and the chemical composition of these nano-objects make them suitable for many applications, ranging from photo-electronic devices[2, 10], to sensors or bio-imaging applications[11].

The semiconductor nanocrystals are called artificial atoms or QDs as a result of the effects of quantum confinement on their electronic spectrum[12, 1]. The QDs can be prepared by various techniques, including Molecular Beam Epitaxy (MBE), lithography, Metal Organic-Chemical Vapor Deposition (MOCVD) and colloidal chemistry[1, 2]. The synthesis of QDs through colloidal chemistry in solution provides significant advantages for the fabrication of nanometer sized building blocks and, ultimately, for the fabrication of devices[13, 2]. A first advantage is that these synthetic methods are not very expensive, in comparison to

MBE for instance. Furthermore, a variety of materials can be synthesized. Not only homogeneous structures can be grown but also heterogeneous structures such as core-shell nanocrystals. Finally, the growth of new nanostructures can be explored at a face pace, in contrast to the much less versatile physical MBE methods, whose growth chambers are usually dedicated to one type of materials.

Following the synthesis of these quantum confined materials, proper methods of characterization have to be devised. While optical spectroscopy is commonly employed to characterize the electronic spectrum of QDs, we believe that the Electron Tunneling Spectrum (ETS) is a more relevant characterization when the goal is to introduce the QDs into electron conducting devices. Indeed, the ETS provides a good measure of the Density of States (DOS) and consequently, a proper characterization of the effects of quantum confinement in the QDs. In the bulk, the DOS is a smooth function of the energy. However, in QDs, the DOS becomes a discontinuous function of the energy.

The scanning Tunneling Microscope (STM) provides a first method to measure the ETS of QDs, this instrument has been employed many times in the past ten years[14–19]. In contrast, on-chip tunneling spectroscopy of colloidal QDs has been employed only a few times. This last method presents several advantages though: (1) The junction is highly stable at low temperature, which allows high resolution measurements of the elastic and inelastic ETS. (2) Gate effects on the QDs can be measured. Today, the nanogaps circuits, a nanogap consists in two electrodes separated by a nanometric distance ($\sim$ 10 nm), can be fabricated by standard e-beam lithography, thermal evaporation and lift-off. The development of on-chip spectroscopy has been hampered by the difficulty of trapping a single colloidal QD into the nanogap. In the past, the strategy employed by different

groups to trap a single nanoparticle within a nanogap was to use self-assembly methods based on molecular or electrostatic interactions. However, several experiences in the group lead to the conclusion that most of these methods were no more efficient than pure random deposition. For this reason, most groups employing those methods had to fabricate and measure hundreds of samples before getting a good one. Facing this situation, our group developed a new method with the goal of detecting in real time the trapping of a single nanoparticle within a nanogap.

In this method, as described in previous publications[20–22], the chip is maintained in a high vacuum box (10^{-6} mbar) and the QDs are projected through a fast pulsed valve from a colloidal solution. After each projection, the tunneling current across the nanogaps is measured to check for the presence of a QD within the nanogap. The cycle of projection is repeated until one QD is trapped in the nanogap, which lead to a sharp increase of the current between the electrodes. This sharp increase of the current is detected by the measurement setup which reacts by stopping the projection system. Using this method, we have fabricated, in the group, junctions with different nanoparticles systems, e.g. Au nanoparticles[20], Fe_3O_4 nanoparticles[21], PbS QDs[22] and HgSe QDs. These last two studies constitue the core of this thesis manuscript and are described in chapter 4 and chapter 5, respectively. In this study of PbS QDs, we have observed three distinct signatures of strong electron-phonon coupling in the ETS. In the shell-filling regime, the 8 times degeneracy of the electronic levels is lifted by the Coulomb interactions and allows for the observation of phonon sub-bands that result from the emission of optical phonons. At low bias, a gap is observed in the ETS that cannot be closed with the gate voltage, which is a distinguishing feature

of the Franck-Condon (FC) blockade. From the data, a Huang-Rhys factor in the range 1.7 to 2.5 is obtained. Finally, in the shell tunneling regime, we found the optical phonons in the inelastic ETS d^2I/dV^2.

To improve the projection system based on a fast pulsed valve, we developed another system based on the electrospray technique. The ElectroSpray Ionization (ESI) deposition process is based on: the charging of the nanoparticle solution passing through an injector needle, the formation of a spray of charged droplets, the transfer of these charged droplets through several chambers of decreasing pressures, and, finally, the deposition of the charged nanoparticles on the chip circuit. We employed this ESI to fabricate HgSe QDs junctions described in chapter 5. With these junctions, we studied the evolution of the tunneling spectrum as the QD occupation level is changed by gating. In the depleted QD, the inter-band gap is observed while in the charged QD, the intra-band gap is observed. Furthermore, we attempted the first measure of the photocurrent across a single colloidal QD.

Chapter 2

State of the art

2.1 Basic concepts

2.1.1 Quantum tunneling

Quantum tunneling is a microscopic phenomenon where a particle can penetrate through a potential barrier even when this barrier is higher than the kinetic energy of the particle. This motion is not allowed by the laws of classical dynamics, but, thanks to the Heisenberg uncertainty principle, this is allowed in quantum mechanics. In a tunnel junction, the tunneling rate can be calculated by using the Fermi's golden rule. This situation is typically described quantum mechanically by a Hamiltonian containing three terms:

$$H_{total} = H_{left} + H_{right} + H_t \tag{2.1}$$

Here H_{left} is the Hamiltonian describing the electrons on the left side of the barrier, H_{right} is the Hamiltonian for electrons on the right side of the barrier,

and H_t is the tunnel Hamiltonian that describes how the left and right electrodes are coupled. If H_t is small enough such that it can be treated as a perturbation, then the Fermi's golden rule can be applied. The tunneling rate is given by:

$$\Gamma_{i\to f} = \frac{4\pi^2}{h}|\langle\Psi_i|H_t|\Psi_f\rangle|^2\delta(E_i - E_f) \tag{2.2}$$

Here Ψ_i is the initial state and Ψ_f is the final state. If the electron tunnels from left to right, then Ψ_i should be an eigenstate of H_{left} and Ψ_f should be an eigenstate of H_{right}. The Dirac delta function, $\delta(E_i - E_f)$, ensure that tunneling occurs only if the initial and final states have the same energy.

If both the left and right electrodes are metallic, then, there will be many initial states and many final states. The total rate will be given by a double sum over all possible initial states and all possible final states. There are so many states in a metal that the double sum can be converted into a double integral over energies. One of the integrals is readily performed using the properties of the delta function. If we write the tunneling matrix element that couples every initial state to every final state as, $|\langle\Psi_i|H_t|\Psi_f\rangle|^2 = T(\varepsilon)$, then the total tunnel current is given by the Landauer formula[1, 2]:

$$I(V) = \frac{2e}{h}\int_{-\infty}^{+\infty} T(\varepsilon)[f_L(\varepsilon) - f_R(\varepsilon)]d\varepsilon \tag{2.3}$$

$$f_L(\varepsilon) = \frac{1}{exp[\frac{\varepsilon-\mu_L-e\phi_L}{k_BT}] + 1} \tag{2.4}$$

$$f_R(\varepsilon) = \frac{1}{exp[\frac{\varepsilon-\mu_R-e\phi_R}{k_BT}] + 1} \tag{2.5}$$

where $f_L(\varepsilon)$ and $f_R(\varepsilon)$ are the Fermi distributions for the electrons in the left electrode (L) and right electrode (R), respectively. V=$\phi_L - \phi_R$ is the bias voltage across the junction and $T(\varepsilon)$ is the transmission coefficient of the junction. All details regarding the physics of the tunneling junction are included in the transmission coefficient. We provide now two different examples where the transmission coefficient can be easily calculated. In the case of a simple tunnel barrier of height $\bar{\phi}$ and width d, the transmission coefficient of the junction can be obtained in the Wentzel-Kramers-Brillouin (WKB) approximation:

$$T(\varepsilon) = exp[-\frac{2d}{\hbar}\sqrt{2m[\bar{\phi} - \varepsilon]}] \tag{2.6}$$

By introducing this transmission coefficient in the Landauer equation, equation 2.3, one gets the formula first obtained by J.Simmons[3]:

$$I = I_0[\bar{\phi}exp[-A\bar{\phi}^{1/2}] - (\bar{\phi} + eV)exp[-A(\bar{\phi} + eV)^{1/2}]] \tag{2.7}$$

$$I_0 = \frac{e}{4\pi^2\hbar(\beta d)^2} \tag{2.8}$$

$$A = \frac{-2\beta d\sqrt{2m}}{\hbar} \tag{2.9}$$

where $\beta \sim 1$. In the low voltage limit, when the tunnel barrier is rectangular, this last formula can be written as:

$$I = \frac{e^2\sqrt{2m\phi}}{h^2 d}Vexp[-\frac{2}{\hbar}\sqrt{2md\bar{\phi}}] \tag{2.10}$$

which shows that the tunnel junction has a Ohmic behavior at low voltage, i.e. the tunnel current increases linearly with the voltage, I $\sim$ V, as shown in figure 2.1, where it can be seen that the differential conductance dI/dV is constant and featureless at low bias. This formula also shows that the current decreases exponentially with the distance, I $\sim$ exp(-βd), where the attenuation coefficient $\beta_0 \sim 1$Å for a tunnel barrier of height $\bar{\phi} = 1$ eV.

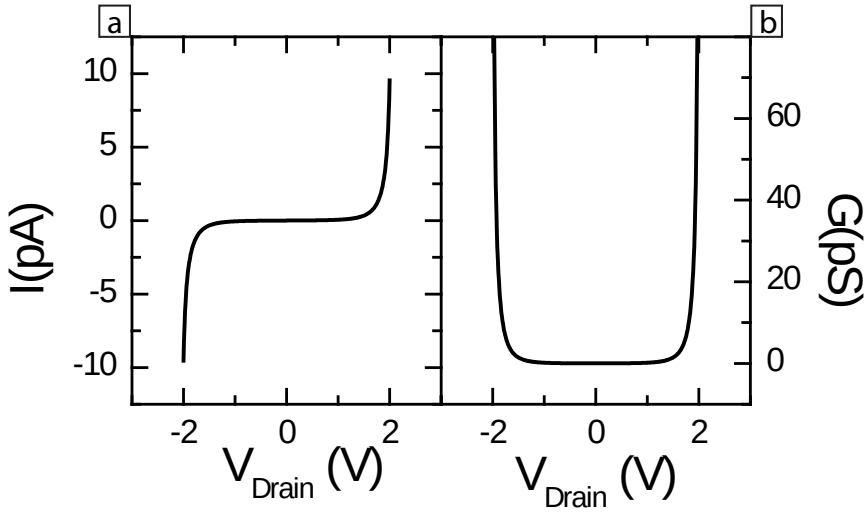

Figure 2.1: (a) Electron tunnel characteristics I$\sim$V for a tunnel junction with a rectangular potential barrier described by the WKB approximation. (b) Corresponding differential conductance dI/dV.

At high voltage, when the barrier becomes triangular, the Simmons's formula can be written in the Fowler-Nordheim forms:

$$I \propto V^2 exp[\frac{-4d\sqrt{2m\bar{\phi}^3}}{3\hbar eV}] \tag{2.11}$$

In more complicated cases, as when a nanoparticle or a molecule is present within the tunnel junction, a more powerful formalism to calculate the transmis-

sion coefficient, such as the Non-Equilibrium Green Function (NEGF) formalism, must be employed. The NEGF formalism can be associated with a structure determination method such as the Density Functional Theory (DFT), to allow precise calculations of electronic transport in molecular system or QDs. In the NEGF formalism, the tunneling current through the double barriers junction is still written using the Landauer formula, equation 2.3, but the coefficient of transmission is given by:

$$T(\varepsilon) = -\frac{1}{\pi} Tr(\frac{\Gamma^L(\varepsilon)\Gamma^R(\varepsilon)}{\Gamma^L(\varepsilon) + \Gamma^R(\varepsilon)} Im[G^r(\varepsilon) - G^a(\varepsilon)]) \tag{2.12}$$

$$g(\varepsilon) = -\frac{1}{\pi} Im[G^r(\varepsilon) - G^a(\varepsilon)]) \tag{2.13}$$

where the Green function $G^r(\varepsilon)$ and $G^a(\varepsilon)$ describe the electron states of the nanoparticle at the center of the junction. The function $g(\varepsilon)$ represents the spectral function, i.e. density of states, of the nanoparticle, while $\Gamma^L(\varepsilon)$ and $\Gamma^R(\varepsilon)$ describe the coupling of the nanoparticle with the left and right electrodes, respectively. In the simple case where a single electronic level exists in the nanoparticle at the energy ε_0 which is described by the Green function:

$$G^{r,a}(\varepsilon) = \frac{1}{\varepsilon - \varepsilon_0 + i\Gamma/2} \tag{2.14}$$

the spectral function will be:

$$g(\varepsilon) = \frac{\Gamma}{(\varepsilon - \varepsilon_0)^2 + (\Gamma/2)^2} \tag{2.15}$$

and the transmission coefficient is:

$$T(\varepsilon) = \frac{\Gamma_L \Gamma_R}{(\varepsilon - \varepsilon_0)^2 + (\Gamma/2)^2} \tag{2.16}$$

$$\Gamma = (\Gamma_L \Gamma_R)/(\Gamma_L + \Gamma_R) \tag{2.17}$$

In this case, the transmission coefficient is a Lorentzian centered on the energy ε_0 of width Γ, as shown in figure 2.2. When this formula is used to describe electronic transport through a molecule , then ε_0 represents the energy of Highest Occupied Molecular Orbital (HOMO) or Lowest Unoccupied Molecular Orbital (LUMO) of the molecule. Calculating the I-V characteristic and the corresponding dI/dV differential conductance, one can see figure 2.2 that a single electronic level at the energy ε_0 that give rises to a peak in the transmission coefficient will also provides a peak in the differential conductance. This is the reason why the Electron Tunneling Spectrum (ETS) is such an interesting characterization of the electronic properties of the nanoparticles, where the differential conductance dI/dV can be interpreted in the first approximation as the density of states in the nanoparticle.

To finish, it should be noticed that two distinct regimes of tunneling can be distinguished, depending on the ratio of tunneling rates, Γ_{in}/Γ_{out}, where the tunneling rate Γ_{in} is the tunneling for electrons entering the island, Γ_{out} is the tunneling rate for electrons escaping the island. The regime $\Gamma_{in} < \Gamma_{out}$ is called shell-tunneling regime, the regime $\Gamma_{in} > \Gamma_{out}$ is called the shell-filling regime.

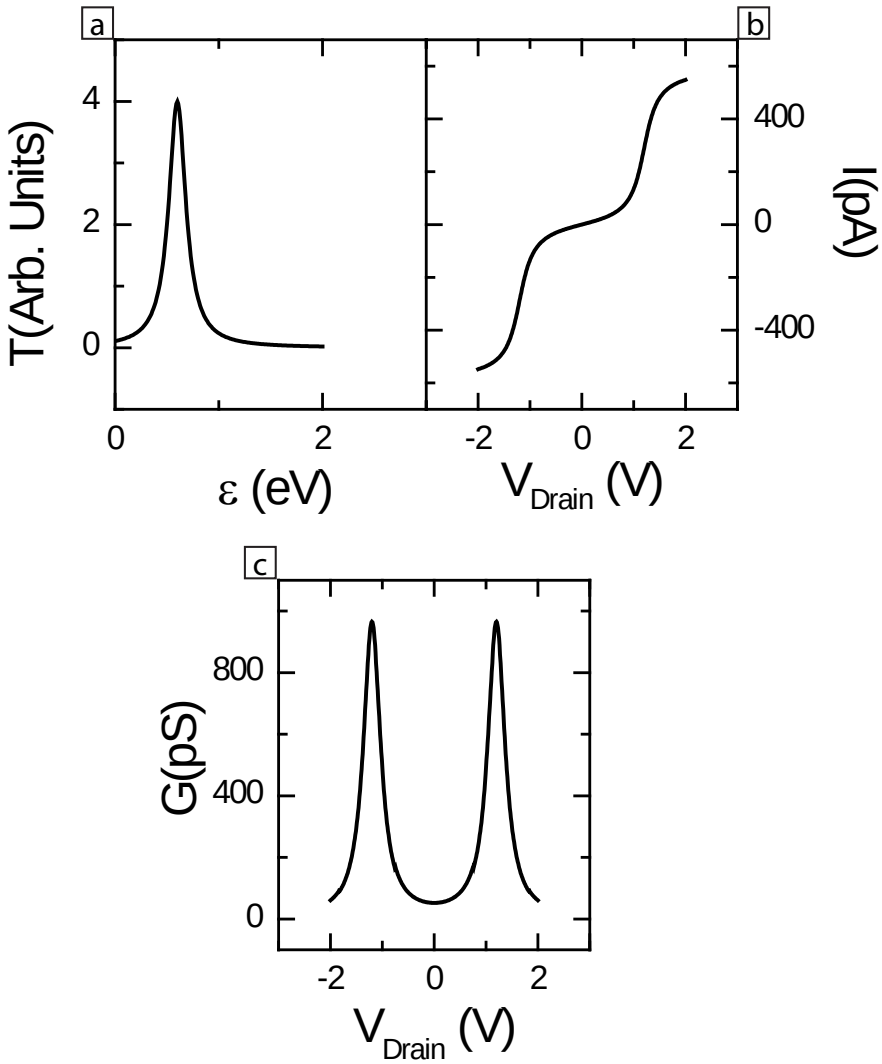

Figure 2.2: (a) Transfer function for a tunnel barrier containing a single electronic level at the energy ε_0 described by the Green function, equation 2.16. A Lorentzian peak is present at the energy ε_0. (b) Corresponding current-voltage characteristic. (c) Corresponding differential conductance. One can see that the peak in the transmission coefficient leads to a corresponding peak in the differential conductance.

2.1.2 Coulomb blockade

For double tunnel barriers junctions, electronic transport from source to drain through a nanoparticle, i.e. nanoparticle, implies necessarily charge variations in the nanoparticle of the amount of at least a single charge e. When the size of the nanoparticle is small enough, the effect of this excess electron can be large enough to react back on the tunneling probability of another electron. This charge feedback is called Coulomb blockade effect which has been found in the early 50's by Gorter. The Coulomb blockade can take place not only in metal and semiconductor islands where the charge carriers are electrons and holes but also in superconductor islands in which the charge carriers are Cooper pairs.

Charging an island , whose capacitive coupling with the neighboring electrodes is given by C, with an electron of charge e requires the Coulomb energy:

$$E_c = \frac{e^2}{2C} \tag{2.18}$$

The Coulomb blockade model is only valid if electron states are localized on the island. This implies that the tunnel resistance between the nanoparticle and the electrodes be sufficiently high. A estimation of the minimum resistance required can be obtained by considering the Heisenberg energy uncertainty:

$$\Delta E \Delta t > \frac{h}{4\pi} \tag{2.19}$$

where $\Delta E = E_c$ is given by the Coulomb energy and the characteristic time for charge fluctuation, Δt, is given by the time required for charging a capacitance C through a tunnel resistor R_T:

$$\Delta t = R_T C \tag{2.20}$$

These relations lead to the minimum tunnel resistance for the existence of the Coulomb blockade, which is:

$$R_T > \frac{h}{2\pi e^2} = 4.1 k\Omega \tag{2.21}$$

In addition, the Coulomb blockade energy must far exceed the energy of thermal fluctuations, i.e.,

$$E_c \gg k_B T \tag{2.22}$$

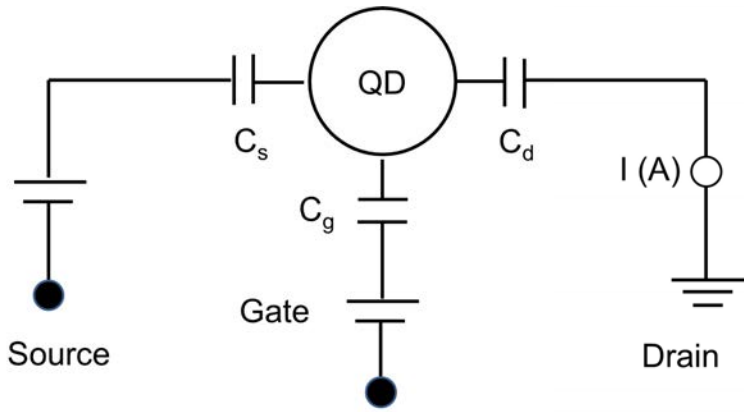

Figure 2.3: The equivalent circuit of a single electron transistor.

In presence of Coulomb blockade, the number of electrons in a metallic island or a semiconducting QD can be controlled by the application of a gate voltage. An island, connected to two electrodes, whose electron occupation number is controlled by a gate voltage, is called a Single Electron Transistor (SET). The Constant Interaction (CI) model[4] provides an approximate description of the

Coulomb blockade effect in QDs. The CI model is based on two important assumptions. First, the Coulomb interactions of an electron in the QD with all other electrons, inside and outside the QD, are parameterized by a constant capacitance C. Second, the discrete electronic energy spectrum, calculated for non-interacting electrons, is unaffected by the Coulomb interactions. The equivalent circuit of a SET is shown in figure 2.3. The CI model approximates the total ground state energy, U(N), of a QD occupied by N electrons with the formula:

$$U(N) = \frac{(e(N - N_0) - C_g V_g)^2}{2C} + \sum_N E_{n,l}(B) \tag{2.23}$$

where N=N_0 for $V_g = 0$ V. The term $C_g V_g$ is a continuous variable and represents the charge that is induced on the QD by the gate voltage, V_g, through the gate capacitance, C_g. The total capacitance between the QD and the source, drain and gate is C=$C_s + C_d + C_g$. The last term of equation 2.23 is a sum over the occupied states, $E_{n,l}(B)$, which are solutions of the single-particle Schrodinger equation. The electrochemical potential of the QD is defined as μ_{QD}(N)=U(N)-U(N-1). Electrons can flow from left to right when μ_{QD} is between the potentials, μ_{left} and μ_{right}, of the leads where eV_{Drain}=μ_{left}-μ_{right}, i.e., $\mu_{left} > \mu_{QD}$(N) $> \mu_{right}$. For small voltages, $V_{Drain} \sim 0$, the Nth Coulomb peak is a direct measure of the lowest possible energy state of an N-eletron, i.e., the ground state electrochemical potential μ_{QD}(N). From equation (2.23) we obtain:

$$\mu_{QD}(N) = (N - N_0 - \frac{1}{2})E_c - \frac{C_g}{C} eV_g + E_N \tag{2.24}$$

where E_N is the energy of the top most filled single-particle state for a N-electron QD. From this last relation, one can obtain the so-called addition energy:

$$\begin{aligned}\Delta\mu(N) = \mu_{QD}(N+1) - \mu_{QD}(N) &= U(N+1) - 2U(N) + U(N-1) \\ &= E_c + E_{N+1} - E_N = \frac{e^2}{2C} + \delta\end{aligned} \tag{2.25}$$

where δ is the energy difference between two quantum states. The related atomic energies are defined as A=U(N)-U(N+1) for the electron Affinity and I=U(N-1)-U(N) for the Ionization energy. Their relation to the addition energy is $\Delta\mu$(N)=I-A. The electrochemical potential of a QD is changed linearly by the gate voltage with the proportionality factor α=C_g/C. The α-factor also relates the peak spacing in the gate voltage to the addition energy:

$$\Delta\mu(N) = e\alpha(V_g^{N+1} - V_g^N) \tag{2.26}$$

where V_g^N and V_g^{N+1} are the gate voltages of the Nth and (N+1)th Coulomb blockade peaks, respectively.

2.1.3 Tunneling spectroscopy

The properties of QDs can be characterized by optical absorption spectroscopy or fluorescent spectroscopy, however, the Electron Tunneling Spectrum (ETS) is a more relevant characterization when the goal is to introduce the QDs into electron-conducting devices.

The Scanning Tunneling Microscope (STM) provides one method of measuring the ETS of single QDs. STM characterization of QDs have been reported previously[5–10]. In those experiments, the QDs are dispersed on a conducting substrate[11], the ETS of QDs is obtained by measuring the conductance between

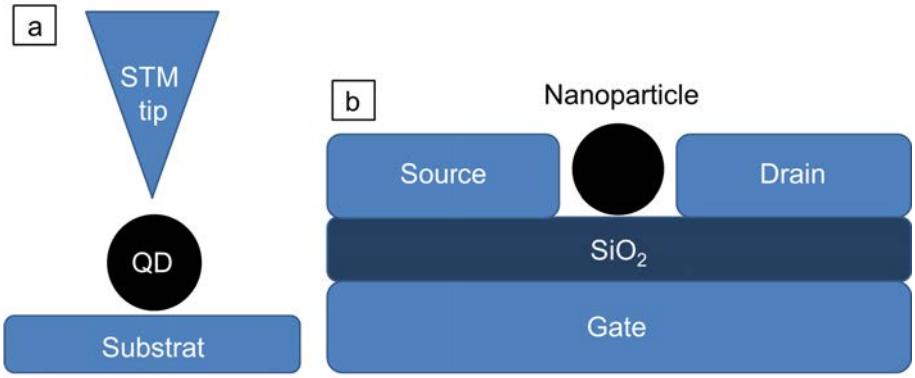

Figure 2.4: (a) The schematic of single QD ETS measurement with STM. (b) The schematic of a single nanoparticle junction on a chip circuit.

the STM tip and the substrate. A schematic of STM spectroscopy measurement is shown in figure 2.4 a.

While STM has been employed several times to study the ETS of colloidal QDs systems, on-chip tunneling spectroscopy of colloidal QDs has been employed only a few times[12–14]. The principle of the experiment is to trap a colloidal nanoparticle (metallic or semiconducting) between two metallic electrodes, as shown in figure 2.4 b. This method of on-chip tunneling spectroscopy presents several advantages: (1) The junction is highly stable at low temperature, which allows high resolution measurement of the elastic and inelastic ETS. (2) A gate electrode can be introduced to fabricate a SET (figure 2.4 b).

2.2 Band structure of semiconducting QDs

2.2.1 Density of states

When the radius of QDs is smaller than the Bohr radius, the electronic spectrum of the QDs is discrete instead of continuous, this effect is called quantum confinement[15–17]. The exciton Bohr radius of a QD is given by:

$$R_{ex} = \frac{\hbar^2 \varepsilon_r \varepsilon_0}{e^2}(\frac{1}{m_e^*} + \frac{1}{m_h^*}) \tag{2.27}$$

where ε_r is the relative dielectric constant of the QD, $\varepsilon_0 = 8.85 \times 10^{-12}$ F/m is the absolute permittivity of vacuum, m_e^* and m_h^* are the electron and hole effective masses, respectively.

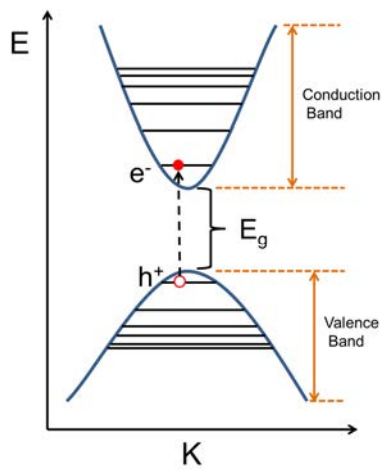

Figure 2.5: Schematic of the band structure of a bulk semiconductor (blue lines) and discrete energy levels for QDs (black lines).

The energy spacing between discrete energy levels, shown in figure 2.5, depends on the QDs size, which can be controlled easily by colloidal chemistry,

leading to the possibility of band gap engineering[18, 19]. The effect of quantum confinement is visible in the electronic DOS which is the density of available states per unit energy[16, 15]. As shown in figure 2.6, in a bulk semiconductor, the electronic DOS, $g(\varepsilon)$, in three dimensions (3D) is directly proportional to the square root of the energy:

$$g(\varepsilon) = \frac{1}{2\pi^2}(\frac{2m^*}{\hbar^2})^{3/2}\sqrt{\varepsilon} \tag{2.28}$$

which is a continuous function of energy. Upon doping the bulk semiconductor, the Fermi level moves into the conduction band. Because of the continuous DOS, electronic transport becomes possible and the semiconductor behaves as a metallic system. Reducing the dimensionality of the system to 2D, e.g. as in a quantum well where the electrons are confined in one direction and free to move in the two other spatial dimensions, the DOS exhibits a stair-like evolution with the energy. At each step, the change in the DOS is given by:

$$g(\varepsilon) = \frac{m^*}{\pi\hbar^2} \tag{2.29}$$

These equal height steps correspond to the quantized electronic levels in the direction of confinement. In a 1D system, for example in nanowires, the electron is only free to move along one direction, the DOS resembles to an array of spikes separating the sub-bands. Within each sub-band, the DOS decreases with the energy as:

$$g(\varepsilon) = \frac{1}{\hbar\pi}\sqrt{\frac{m^*}{2E}} \tag{2.30}$$

For 0D systems, such as QDs, where the electron is confined in the three spatial dimensions, the DOS is described by a comb of δ-functions[20, 16]. The electron confinement produces a series of discrete energy levels, which provides the atomic-like behavior to the QDs and their unique optical and electrical properties[21, 22].

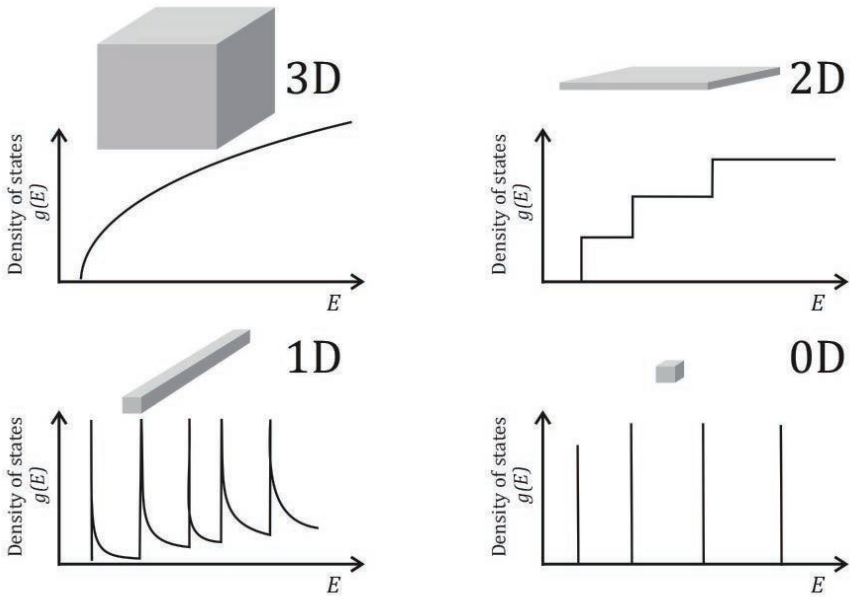

Figure 2.6: The schematic representation of DOS for 3D, 2D, 1D and 0D system.

2.2.2 Band structure of PbS QDs

This thesis presents the investigation of electron tunneling spectrum as well as the fabrication of the corresponding devices for PbS and HgSe QDs. In this section, I will introduce the band structure of those QDs. PbS belongs to the class of IV-VI semiconductors with narrow band gap and small electron and hole effective masses, $m^*_{e(h)} \sim 0.08m_0$, where m_0 is the electron mass in vacuum. The small and almost equal electron and hole effective masses lead to a large Bohr radius

$\sim$ 20 nm. Because of this large Bohr radius, the electrons, holes and excitons are strongly confined[23]. Thus, the band gap in these QDs can be size tuned on a large energy range which make them suitable for various applications, such as, near-infrared detectors[24], solar cells[25, 26] and LEDs[27].

Bulk PbS has a narrow band gap, $E_g = 0.286$ eV at 4.2 K and $E_g = 0.42$ eV at 300 K. It has the rock salt structure with a lattice constant a = 5.936 Å and has a large relative dielectric constant $\varepsilon_{PbS} = 170$[23]. The smallest band gap is located at the L point, consequently, the first discrete energy levels $1S_e$ and $1S_h$ are located at the L point[8, 11]. There are four equivalent L point valleys in the Brillouin zone[11], as shown figure 2.7. Including the two-fold spin degeneracy, this implies that the levels $1S_e$ and $1S_h$, are eight times degenerated.

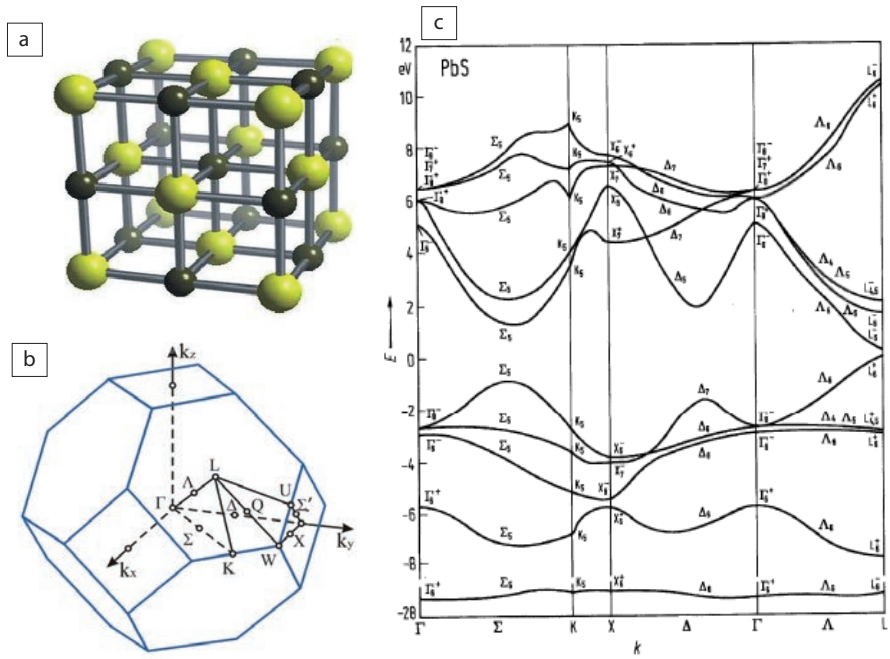

Figure 2.7: (a) Rock salt structure. (b) The schematic of the Brillouin zone of the rock salt structure. (c) Band structure of PbS.

2.2.3 Band structure of HgSe QDs

HgSe belongs to the II-VI semiconductor class, it has the zinc blende structure with a lattice constant a = 5.997 Å and a relative dielectric constant ε_{HgSe} = 25.6, the hole effective mass is m_h^* =0.78m_0 and the electron effective mass is $m_e^* = 0.05m_0$[23]. Bulk mercury chalcogenides have a large mobility about 15000 cm^2/Vs at room temperature[23]. The band structure of HgSe has been subject to debate[29] as a consequence of the controversial result based on angle-resolved photoemission spectroscopy by Gawlik et al[30]. The consensus about the band structure of HgSe, shown in figure 2.8 c, is that HgSe is a zero gap semiconductor[28] with an inverted band structure. The band structure was obtained from magneto-absorption measurements, optical experiments and theoretical calculations[31]. The Hg s level forms a state of Γ_6 symmetry (with space for two electrons) at the Brillouin zone center. This state is pulled down below the anionic p-like Γ_8 level due to the large effective positive charge of the Hg core. Because the number of valence electrons is sufficient to occupy only two of the four levels of Γ_8 character, the unoccupied Γ_8 levels become part of the conduction band, which consequently becomes degenerate with the valence band maximum at Γ point, creating a zero energy gap[29].

Because of their inverted band structure, the mercury chalcogenides, HgSe and HgTe, attracted an intense interest recently with the search for topological materials[32]. The crystal structure, Brillouin zone and band structure[28] of HgSe are shown in figure 2.8. It should be noticed that despite the apparent strong similarities between HgSe and HgTe, an important difference exists. As shown by DFT calculations, [33], for HgSe, the Γ_6 band is also below the Γ_7 band,

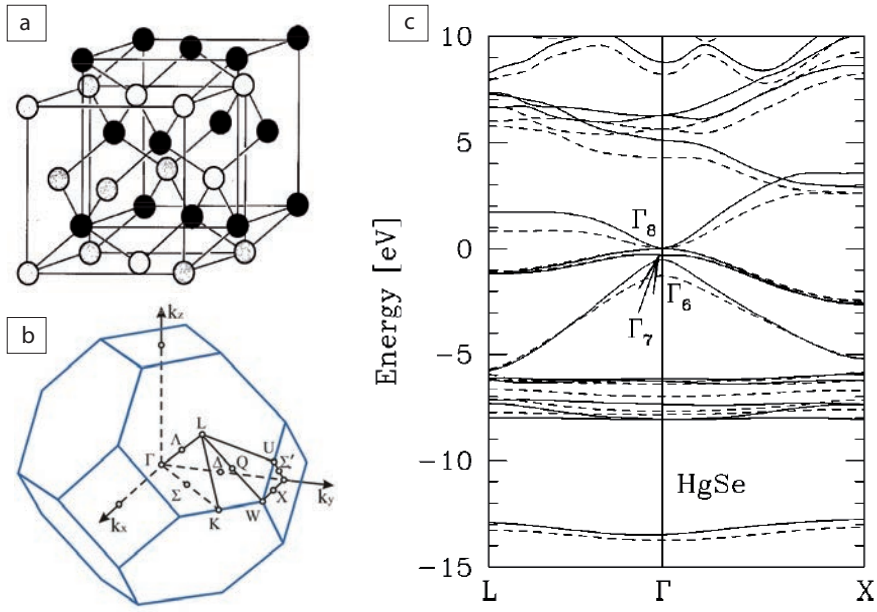

Figure 2.8: (a) The schematic of zinc blende structure. (b) The schematic of Brillouin zone for zinc blende structure. (c) The band structure of HgSe, as calculated with GW approximation (solid lines) and density-functional-theory calculation within the local-density approximation (dash lines), respectively[28].

unlike HgTe. Figure 2.9 shows the calculated band structure of HgTe and HgSe extracted from Ref.[33]

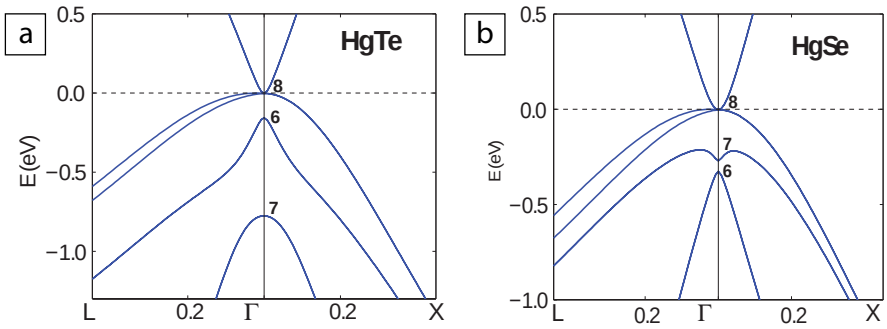

Figure 2.9: Band structure of (a) HgTe and (b) HgSe using the *hybrid* quasi-particle self-consistent GW (QSGW) approximations (G: Green's function; W: screened Coulomb interaction)[33]. Both systems have an inverted band structure. In HgTe, the band Γ_6 is below the bandΓ_8. In HgSe, the band Γ_6 is below both bands Γ_7 andΓ_8.

2.3 Examples of tunnel spectroscopy in different QD systems

As we already mentioned earlier, different strategies can be employed to fabricate quantum confined materials and devices. These different methods and materials produce QDs with distinct spectral characteristics. The most two important parameters that characterized the spectral properties of the QD are the Coulomb energy, $E_c = e^2/r$, which is inversely proportional to the radius of the QD and the mean level spacing $\delta = 1/(g(\varepsilon_F)r^3)$, which is inversely proportional to the product of the density of states and the volume of the QD.

From these two relations, different regimes can be distinguished. When the

density of states is large as in metals, the addition spectrum of the QD will be mostly controlled by the Coulomb energy. This regime occurs in metallic nanoparticles or in large microfabricated semiconducting QDs with the Fermi level in the conduction band.

This can be seen by considering the ratio $\delta/E_c \sim 1/r^2$. At large r, this ratio becomes much smaller than one, indicating that the Coulomb energy dominates the addition spectrum for large r. For small QDs, in contrast, the mean level spacing δ is the largest energy scale. This regime happens in colloidal QDs or in molecules.

The distribution of the electronic levels is another major difference that distinguishes small from large QDs. In small colloidal QDs or in molecules, where the mean level spacing is large, the electronic levels are distributed according to a shell structure, similar to atoms, with levels labeled by a principal quantum number (n=1, 2, ...), an orbital number S, P, D, ..., and eventually magnetic and spin numbers. In this case, the electronic level distribution follows a regular pattern that can be precisely calculated, for example with the **k.p.** theory.

In large semiconducting QDs or in metallic nanoparticles where the mean levels spacing is small and the Fermi wavelength is smaller than the size of the QD, the distribution of the electronic levels is random and is described by the random matrix theory.

To illustrate this presentation, I provide below different examples of the tunnel spectroscopy of QDs in different regimes.

2.3.1 Microfabricated large QDs

One of the first method to fabricate SET employed microfabrication techniques and 2D electron gas forming at the interface of III-V heterostructures. L. Kouwenhoven et al[4]., fabricated the pillar structure QD SET shown in figure 2.10 a. The QD of the heterostructure is formed in the central well made of undoped $In_{0.05}Ga_{0.95}As$ and has a thickness of 12 nm. Undoped $Al_{0.22}Ga_{0.78}As$ layers form the tunneling barriers. The upper barrier has a thickness of 9 nm and the lower barrier is 7.5 nm thick. The conducting source and drain contacts are made from Si-doped $n-GaAs$. The metal electrode around the pillar is used to apply the gate voltage. The measurements are performed at a temperature of 200 mK.

Figure 2.10 c shows a color plot of the differential conductance dI/dV as function of gate voltage and drain bias. The white diamond areas correspond to the regions of Coulomb blockade, $dI/dV = 0$. While for colloidal QDs the Coulomb energy is mostly determined by the self-capacitance, C_{self} =$4\pi\varepsilon_0\varepsilon_r$r, for large microfabricated QDs, the capacitance coupling with the electrodes is large and, consequently, the Coulomb energy is determined by the total capacitance C= $C_s+C_d+C_g$. In this microfabricated QD, because the Debye length is smaller than the size of the QD, upon charging with the gate voltage, the screening length decreases and, consequently, the capacitance between the QD and the electrodes increases. As $E_c \sim e^2/C$, the Coulomb energy decreases upon increasing the gate voltage as shown in figure 2.10 c. The decrease of the Coulomb energy upon increasing the gate voltage is a characteristic behavior of large microfabricated QDs.

From the figure 2.10 c, one can extract the mean level spacing, δ, as the

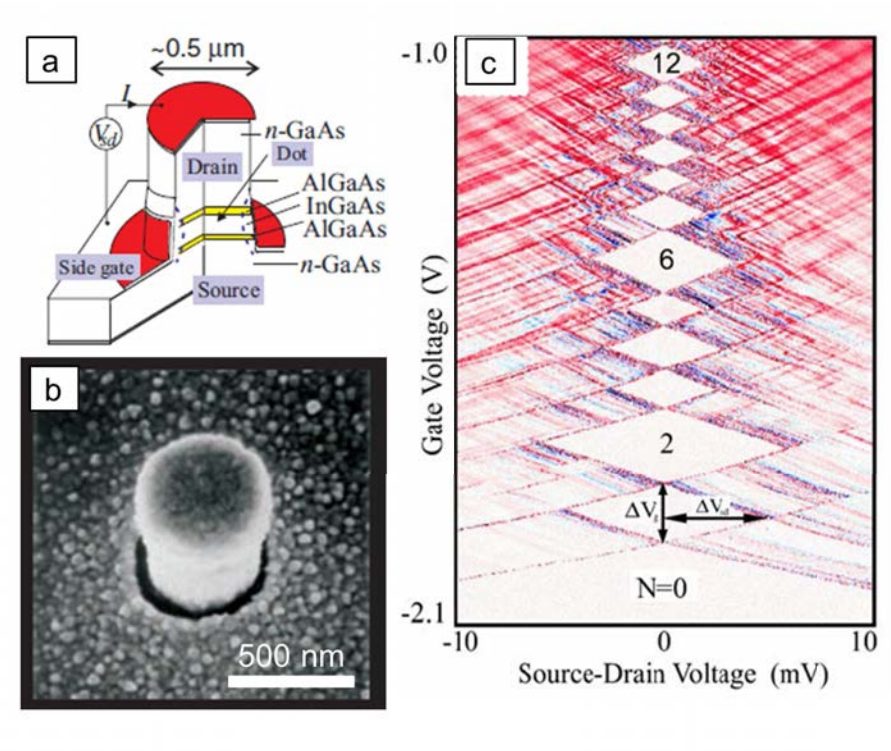

Figure 2.10: (a) The schematic of the semiconductor heterostructure. The dot is located between the two AlGaAs tunneling barriers. A negative voltage applied to the side gate squeezes the dot thus reducing the effective diameter of the dot (dashed line). (b) SEM image of the QD pillars device. (c) The differential conductance, dI/dV, plotted on a color panel. The white regions correspond to Coulomb diamonds, dI/dV=0. Red indicates positive conductance while blue indicates negative conductance.

distance between the thin red lines, and we obtain $\delta \sim 1$ meV. This mean level spacing is about one order magnitude larger than in metallic nanoparticle, but remains very small in comparison to the colloidal QDs. Furthermore, in this microfabricated QD, the electronic levels do not seem to follow a shell distribution, instead, they seem to be randomly distributed.

2.3.2 Nanotubes and nanowires based QDs

Another way to microfabricate QDs is to start from synthesized nanowires such as semiconducting InAs nanowires or carbon nanotubes. R. Leturcq et al[34]., fabricated a QD junction from a suspended single-wall carbon nanotube, a SEM image of which is shown figure 2.11. In this method, the QD is formed by a local gate electrode. The QD induced in the nanotube is 'naturally' separated from the other parts of the nanotube by tunnel barriers. Figure 2.11 b shows that the Coulomb diamonds have a four-fold symmetric dependence with the gate voltage due to the four-fold degeneracy of the electronic states of the QD. The figure 2.11 c shows a zoom on the tip of one of the diamonds, where phonon sub-bands are observed at the edges of the diamonds. Actually, in this nanotube QD, the electrons are not coupled to phonons modes but instead to vibrons modes of the nanotube itself. Furthermore, it can also be observed that the conductance is suppressed around zero drain bias, and this, for any gate voltage. This behavior has been interpreted as a consequence of the Franck-Condon blockade, which we will describe in more details in the chapter dedicated to the PbS QDs.

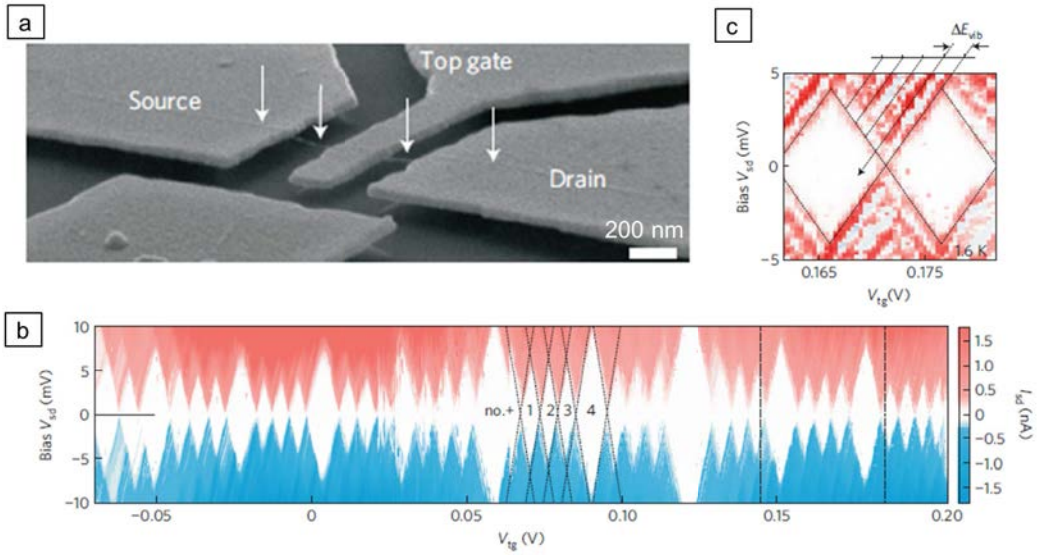

Figure 2.11: Data extracted from ref[34]. (a) The SEM image of the suspended carbon nanotube device. (b) The current I as function of gate and drain voltages, the white regions correspond the Coulomb diamonds which are four-fold periodic. (c) The zoom on the tip of a diamond, the phonon sub-bands are observed at the edge of the diamond.

2.3.3 STM spectroscopy of colloidal semiconducting QDs

Nanocrystals can be obtained easily by colloidal synthesis. Many technologically important metal, semiconducting and even superconducting QDs can be synthesized as uniform sub-20 nm nanocrystals[35]. Small size semiconducting QDs exhibit strong quantum confinement and, consequently, constitute a remarkable play ground for tunneling spectroscopy.

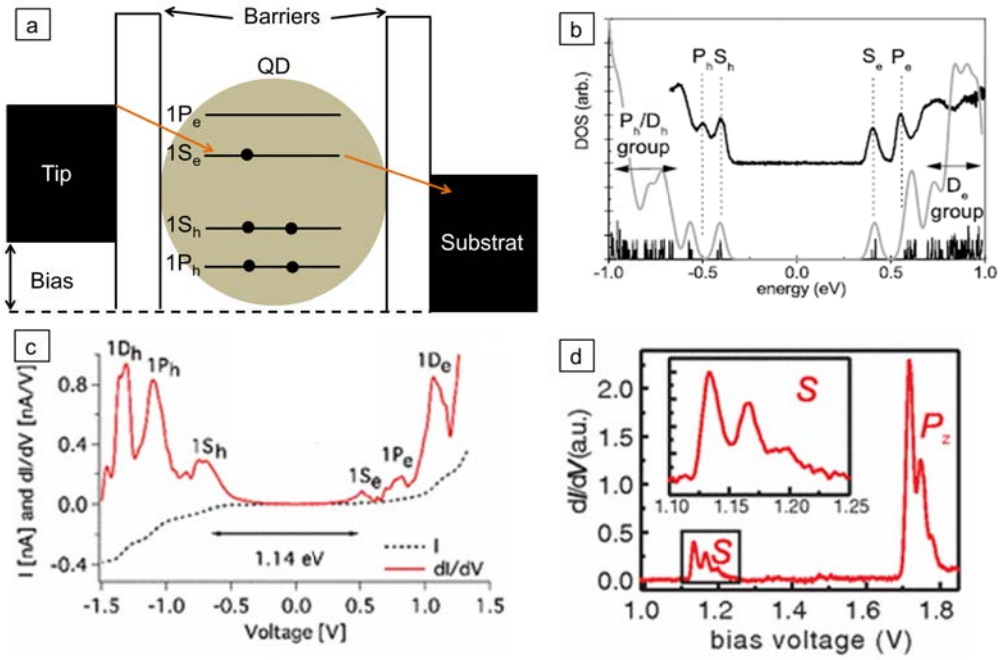

Figure 2.12: (a) The schematic of tunnel processes across discrete energy levels of QD. (b) The conductance curve, dI/dV, as function of bias voltage measured across a single PbSe QD, extracted from ref[11]. (c) The I/V curve, dashed line, and dI/dV curve, red line, measured across a single PbS QD, extracted from ref[8]. (d) The dI/dV curve as function of bias voltage measured across a single CdSe QD of diameter 3 nm. The inset is a zoom on the phonon-induced sub-bands observed on the S state. Those data are extracted from ref[36].

P. Liljeroth et al., measured the ETS of single colloidal PbSe QDs by STM at

5 K[11]. The differential conductance curve, dI/dV, as function of bias voltage, is shown in figure 2.12 b. Since the dI/dV is proportional to the DOS, the discrete energy levels, $1S_e$, $1S_h$, $1P_e$ and $1P_h$ are observed in the dI/dV curve in the shell-tunneling regime.

B. Diaconescu et al., measured the ETS of single PbS QDs by STM at 100 K[8]. The differential conductance curve (red solid line,) and I-V curve (black dashed line) as function of bias voltage are shown in figure 2.12 c. Six discrete energy level, $1D_h$, $1P_h$, $1S_h$, $1S_e$, $1P_e$ and $1D_e$ are observed in the dI/dV curve in the shell-tunneling regime.

Z. Sun et al., measured the ETS of single CdSe QDs by STM at 4.8 K[36]. The differential conductance curve dI/dV as function of bias voltage is shown in figure 2.12 d. In this tunneling spectrum, the 1S and 1P are also visible. Furthermore, as shown in the inset, additional sub-bands appear for each level. These sub-bands are the consequence of the coupling of the electrons with the lattice vibrations, i.e. phonons, of the QD. Indeed, when electrons are interacting with phonons, the discrete electron levels peaks become dressed with additional sub-bands separated by the phonon energy $\hbar\omega_0$, as shown in the inset of figure 2.12 d. The electron-phonon coupling strength is dependent on the electron orbital symmetry, the number of added electrons, and the size and dielectric environment of the QD.

2.3.4 On-chip spectroscopy of colloidal semiconducting QDs

D. Klein et al[14]. fabricated the first on-chip junction with a CdSe QD and measured the ETS of the junction at 5 K. In this device, the gold electrodes are

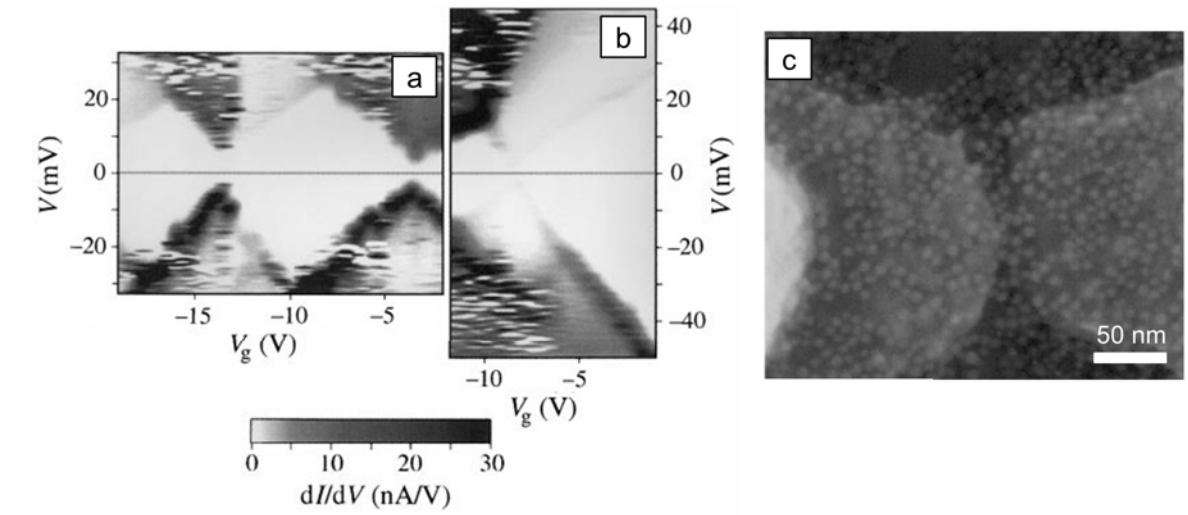

Figure 2.13: (a) and (b) The differential conductance of CdSe QD, dI/dV, as function of drain and gate voltages, the white areas correspond to the Coulomb blockade region. (c) The SEM image of CdSe colloidal QDs deposited on the chip with two electrodes separated by a $\sim$ 10 nm gap.

functionnalized with di-thiol (SH) alkyl molecules. One side of the di-thiol chain is bound to the gold electrode, it is expected that the other side is bound to the QD. As discussed previously, one of the major advantage of on-chip tunneling spectroscopy is to allow the application of a gate voltage, as shown in figure 2.13 a and b. In this figure, the Coulomb diamonds can be observed in ETS. At the most positive gate voltage, the QD is depleted of electrons and the inter-band gap is observed in the ETS. Furthermore, an additional small gap is observed at the degeneracy point of the Coulomb diamonds, a phenomena which may also be related to the Franck-Condon blockade that we observed in the PbS QDs. Surprisingly, the discrete levels 1S, 1P, etc... are not observed in the ETS spectrum of this QD. Since this first experiment, no other on-chip tunneling spectroscopy experiment with colloidal QDs has been reported.

2.3.5 Colloidal metallic nanocrystals

While on-chip tunneling spectroscopy of QDs is rare, on-chip tunneling spectroscopy of colloidal metallic gold nanoparticles is more common[12, 37]. While most tunneling spectroscopy studies of metal nanoparticles could only resolve the effects of Coulomb blockade, the work of F. Kuemmeth et al[12]. is remarkable as it is one of the few works where the discrete electronic level structure of a metallic nanoparticle could be resolved.

F. Kuemmeth et al[12]. fabricated colloidal gold nanoparticles junction by submerging a nanogap covered chip circuit in a gold colloidal solution. The silicon chip circuit was functionalized with positive amine NH_3^+ groups, the nanoparticles were functionalized with negative carboxylic COO^- groups. This functionalization allowed an electrostatic assembly of the nanoparticles on the chip. The figure 2.14 d shows that the gold nanoparticles are distributed on the chip surface, and only one gold nanoparticle contributes to the current between the two electrodes. To resolve the discrete electronic level structure where the mean level spacing is very small, about 100μeV, the ETS had to be measured at very low temperature $T \sim 90$ mK. The Coulomb diamonds are observed in the plot of the differential conductance dI/dV as function of gate and drain bias, figure 2.14 a. The figure 2.14 b is a zoom on the tip of a Coulomb diamond. The bright lines correspond to peaks in the differential conductance, shifting with the gate voltage. These bright lines corresponds to the discrete energy levels of the gold nanoparticle. Figure 2.14 c is a profile as function of drain voltage extracted from figure 2.14 b. Because the gold nanoparticle has a high density of states, the spacing between two peaks is very small, $\delta \sim 300$ μeV. Consequently, the addition energy will be

mostly determined by the Coulomb blockade energy. Furthermore, because the screening length in metallic nanoparticles is very small, the self-capacitance of the nanoparticle will depend only on the size of the nanoparticle. Consequently, the Coulomb energy is independent of the gate voltage, and, for this reason, the Coulomb diamonds have the same size upon increasing the gate voltage, in contrast to the large microfabricated QD where the Coulomb energy decreases upon increasing the gate voltage. Finally, an analysis of the distribution of the electronic levels shows clearly that the levels are not distributed according to a shell structure. Instead, as discussed in Ref.[12], the electronic levels seem distributed according to the random matrix theory.

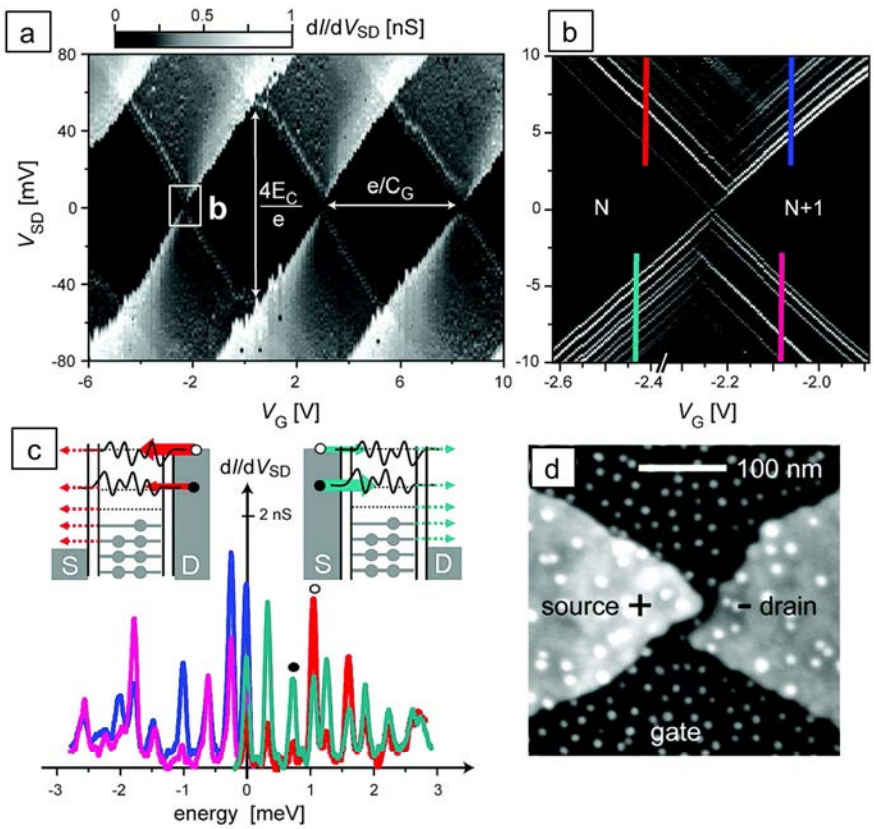

Figure 2.14: (a) The differential conductance, dI/dV, as function of gate and drain bias measured on a colloidal gold nanoparticle single electron transistor. (b) Zoom on the tip of diamond shown in panel a. (c) Line profiles obtained from panel b. (d) SEM image of the colloidal gold nanoparticle single electron transistor in which only one nanoparticle contributes to the current flow between source and drain electrodes.

2.3.6 Conclusion

To conclude this description of different QD systems, we have seen that the electron tunneling spectrum depends on the Coulomb energy, E_c, the mean level spacing, δ, the ratio between these last two quantities and the strength of the electron-phonon coupling. Table 2.1 summarizes the different spectrum patterns expected in the most important categories. In metallic nanoparticle systems, column I of table 2.1, the density of states is large, which implies that the mean level spacing is very small. Because the Fermi wavelength is smaller than the nanoparticle diameter the energy of the electronic levels will be highly sensitive to the disorder in nanoparticle, in particular at the surface, and, consequently, will follow a random distribution as described by the random matrix theory. Furthermore, as the screening length is also smaller than the nanoparticle diameter, the Coulomb energy will not depend on the gate voltage, and the Coulomb diamonds should keep the same size as the gate voltage is increased. In large microfabricated semiconducting QDs, column II table 2.1, the mean level spacing is also small and the electronic levels are also randomly distributed. Two important differences distinguish this type of QDs from the metallic nanoparticles. First, because the screening length is large, comparable to the size of the QD, upon charging the QD, the capacitance coupling of the QD with the electrodes change and so is changing the Coulomb energy. This leads to a spectrum where the size of the Coulomb diamonds decreases upon increasing the gate voltage. Second, because the electron density in the QD is much smaller than in a metallic system, the QD can be depleted with the gate voltage. When this happens, the Coulomb diamond structure disappears and only the inter-band gap appears in

the tunneling spectrum.

Finally, in small colloidal QDs, column III in table 2.1, the mean level spacing is large, usually larger than the Coulomb energy and the Bohr radius is larger than the QD. In this case, the addition energy depends mostly on the inter-level spacing and the electronic levels are distributed along a shell structure, for those states located within a single band. In addition, the energy interval between the electron-type levels and hole-type levels depends on the inter-band gap.

QD systems	Colloidal metallic nanoparticles ($\sim$ 10 nm)	Microfabricated large QDs ($\sim$ 1 μm)	Colloidal QDs ($\sim$ 10 nm)
Mean level spacing δ	$\sim$ 0.1 meV	$\sim$ 1 meV	$\sim$ 100 meV
Coulomb energy E_c	$\sim$ 80 meV	$\sim$ 100 meV	$\sim$ 40 meV
The ratio δ/E_c	$\sim$ 0.0013	$\sim$ 0.01	$\sim$ 2.5
The density of states	High density of states	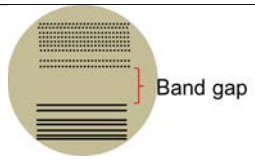 High density of states	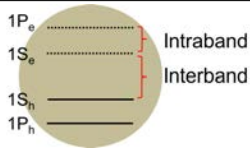 Atomic like (S, P, D)
The shape of Coulomb diamonds	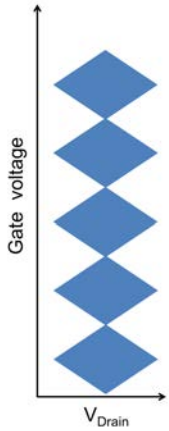	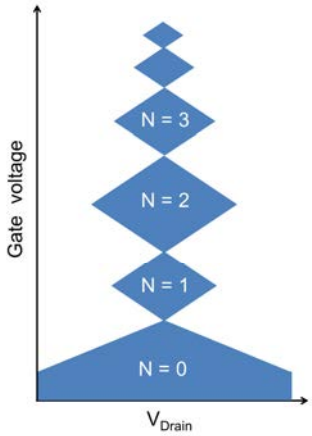	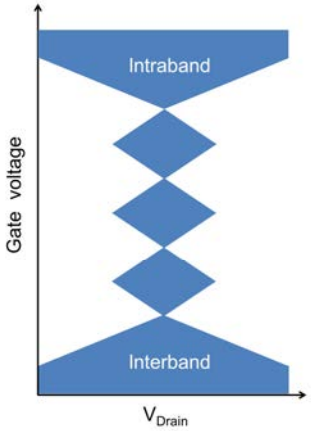

Table 2.1: Comparison of different systems. The unoccupied states are represented by dashed lines and the occupied states are represented by the solid lines. First column: For a metallic colloidal gold nanoparticle, the density of states is large and so the mean level spacing is very small. The screening length is also very small, consequently the Coulomb diamonds are identical to each other. Second column: For a large microfabricated semiconducting QD, the density of states is smaller than a metallic nanoparticle but still much larger than for a colloidal QD. In that case, the distribution of electronic levels follows a random distribution as for metallic nanoparticle. As the screening length is much larger in semiconductor, the size of the Coulomb diamonds shrinks as the gate voltage increases. Third column: For colloidal semiconducting QDs, the mean level spacing is very large and, consequently, the spectrum is mostly determined by the shell distribution of the electronic levels, except when the Fermi level is located on a degenerated level, where Coulomb n-1 diamonds appear, where n is the degeneracy of the electronic level.

Chapter 3

Samples preparation and experimental setups

3.1 Samples preparation

3.1.1 Synthesis of PbS QDs

In a 50 mL three neck flask, 0.44 g of lead oxide (PbO), 2 mL of oleic acid and 10 mL of phenyl ether are heated under argon at 150 °C for 1 h. The final solution is orange red. Meanwhile 32 mg of sulfur are mixed in 2 mL of oleylamine and strongly agitated until full dissolution of the sulfur precursor. The flask is heated at 190 °C and the sulfur mixture is quickly injected. The temperature is set at 180 °C and the reaction is performed for 5 min. The flask is cooled down and the QDs are cleaned using toluene as nonpolar solvent and ethanol as polar solvent.

The PbS cubes have 10 nm edges, as observed through TEM, figure 3.1, and from the width of the diffraction peaks in the XRD, figure 3.2 a, using the Scherrer

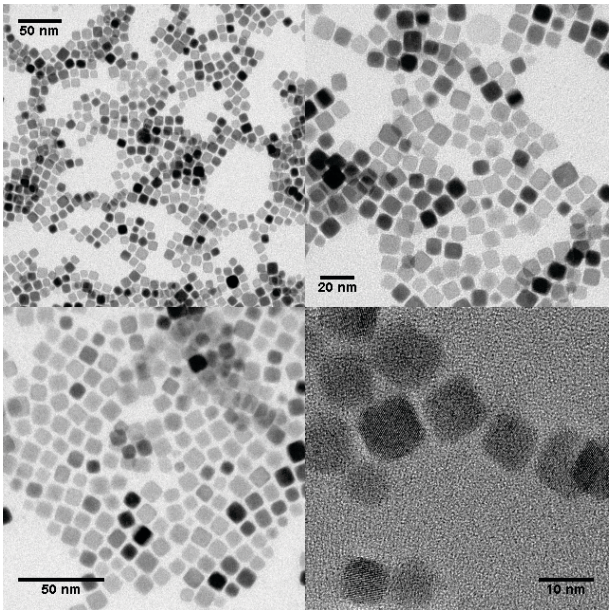

Figure 3.1: The TEM images of PbS QDs.

equation. The XRD diffractogram, figure 3.2 a, is consistent with the rock salt structure. The absorption spectrum, figure 3.2 b, is not very structured but we can estimate the optical gap around 2.3 μm (0.55 eV) with two other features at 2.1 μm and 1.7 μm.

3.1.2 Synthesis of HgSe QDs

In a 100 mL three necks flask, mix 1 g of mercury acetate with 40 mL of oleic acid. The system is degased under primary vacuum for 1 h at 85 °C. In a 25 mL three necks flask on a Schlenk line with a small heating mantle, introduce 12 mL of the mercury oleate solution and 30 mL of oleylamine. Put under vacuum at 85 °C for at least 30 min. Switch the atmosphere to Ar. introduce quickly 0.9 mL of TOPSe 1M. The solution turns dark almost immediately. After 30 min the flask is quenched by adding 1 mL of dodencathiol. The heating mantle is removed and the

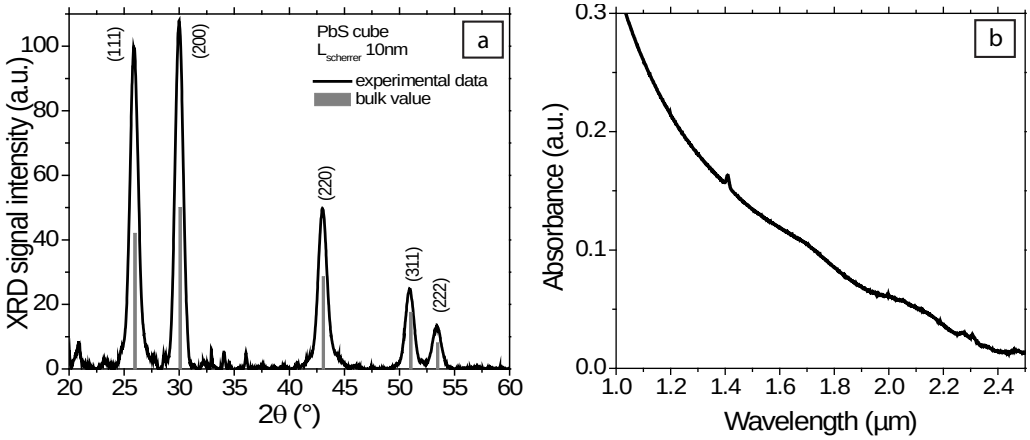

Figure 3.2: (a) The XRD diffraction curve of PbS QDs. (b) The absorption curve of PbS QDs.

solution is let cooled down. The content of the flask is cleaned by adding ethanol and the solution is centrifugated for a few minutes. The formed dark pellet needs to be redispersed in toluene. The cleaning is repeated two more times. The TEM images are shown in figure 3.3, the HgSe QDs are mono-dispersed and the sphere have a size of about 10 nm.

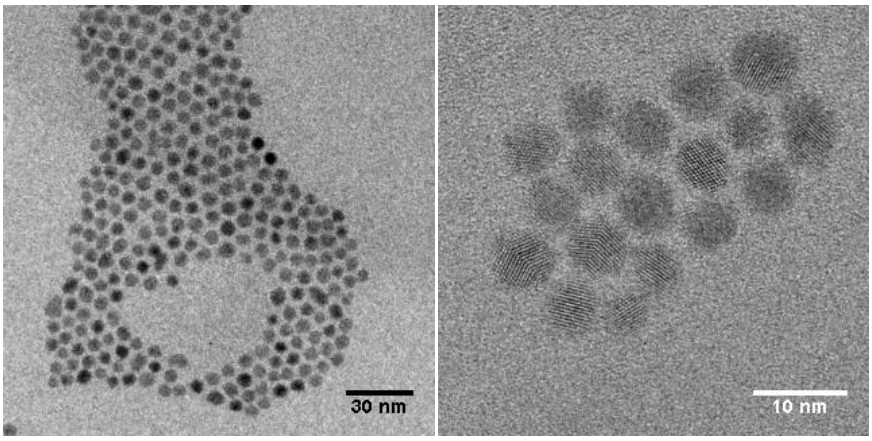

Figure 3.3: The TEM images of HgSe QDs.

3.1.3 Ligands exchange

After synthesis, the colloidal QDs are surrounded by long organic ligands which make them hydrophobic and are usually dispersed in a nonpolar solvent such as toluene. To reduce the width of the tunnel barrier between the QDs and the conducting gold electrodes, it is important to remove the organic ligands. Following the works by the Talapin's group at Chicago which have shown [1] that it was possible to replace the organic ligands by small anions such as S^{2-}, several groups used similar kind of methods for removing the organic ligands. In particular, E. Lhuillier et al. (B. Dubertret's group) working in the laboratory replaced the organic ligands with S^{2-} anions to fabricate transistors and photo-conducting devices[2]. In these devices, a large increase of the conductance is observed after ligands exchange. To realize a ligands exchange[1] as depicted figure 3.4, the solution of colloidal QDs is diluted with hexane to a concentration of 5 mg/mL, then, 1 mL of this colloidal solution is mixed with 1 mL of polar solvent NMF (N-methylformamide) which contains Na_2S (5 mg/mL). The mixture is stirred for 10 min. One minute after stopping stirring, the NMF phase and the hexane phase separate with the QDs having been transferred from the hexane to the NMF as the organic ligands are replaced by the sulfur anions. Then, the NMF phase is extracted and washed with hexane three times to remove any remaining organic ligands. After this washing step, 1 mL of acetonitrile is added to the NMF phase to precipitate the QDs. The precipitate is re-dispersed in NMF and filtered through a 0.22 μm PVDF filter. The QDs dispersion in NMF can be stable for several weeks.

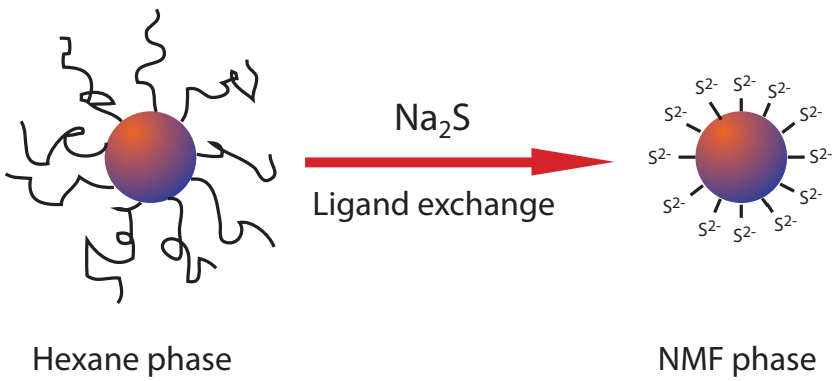

Figure 3.4: Ligands exchange on QDs.

3.1.4 Fabrication of nanogaps circuits

The work performed for thesis required nanogap chip circuits. To that end, we have a collaboration with C. Ulysse from LPN (Marcoussis). He provided us with several wafers of nanogap chip circuits, as depicted figure 3.5. The electrodes of Cr (5 nm)/Au (25 nm) are fabricated by e-beam lithography, thermal evaporation and lift-off. These electrodes are deposited on a p-doped silicon wafer covered by a 300 nm thick silicon oxide layer. The distance between two electrodes is about 10 nm, forming the nanogap within which the nanoparticle will have to be trapped. After deposition of the nanogap electrodes by e-beam lithography, we use optical lithography to pattern the contact electrodes connected to the small nanogap electrodes. One 3 inch wafer contains 36 chips and one chip (8×8 mm) contains 32 nanogaps which consist of 32 drain electrodes and one common source electrodes[3], as shown in figure 3.5.

To prepare a chip for the experiment, one chip cut from the wafer is glued on a ceramic chip holder containing 44 pins. 32 of those pins are connected to the

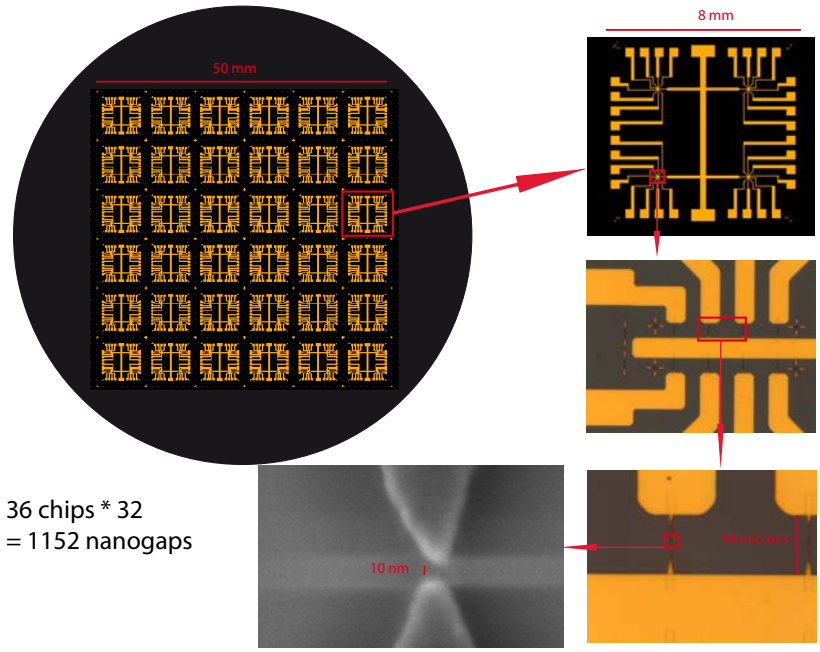

Figure 3.5: A wafer contains 36 chips, each one contains 32 nanogap as shown on the SEM picture.

drain electrodes and one of the pins is connected to the common source electrode. All these connections are made with a wire bonder (Kulicke & Soffa) using Al (diameter=25 μm) wires. Two of those pins are connected to the p-doped silicon substrate with Al wires and silver epoxy , which is used a back gate. The ceramic chip circuit can be installed into a PLCC chip holder, as shown in figure 3.6, which is connected to the measuring instruments.

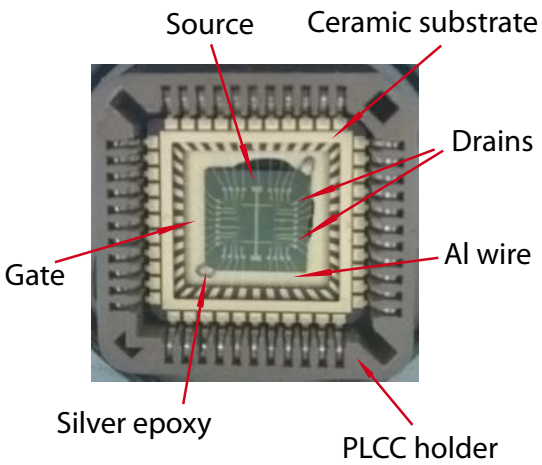

Figure 3.6: The image of a chip installed in a PLCC holder.

3.2 Experimental setups

In order to trap a single nanoparticle within the nanogap, various methods have already been explored by different groups. Most groups employed a similar strategy consisting in functionalizing the nanoparticles and electrodes, such that the nanoparticles will self-assemble within the nanogap circuit. Different types of interactions can be employed such as electrostatic, Van der Waals or covalents interactions. However, after several experiments in the group, it was concluded

that these functionalization methods are barely more efficient the pure random deposition of the nanoparticles on the chip circuit. Furthermore, because these functionalization methods have to be realized in solution, the trapping of the nanoparticle within the nanogap cannot be detected by measuring the tunnel current. Indeed, because of ionic currents, it is almost impossible to measure a tunnel current within a solution. Consequently, to test for the presence of a nanoparticle within the nanogap, the chip circuit has to be dried, which is a delicate step where the nanoparticle can also move. This drying step add an additional random contribution to the placement of the nanoparticle in solution.

Facing this random process, two kind of strategies are possible. Either, we could fabricate and measure hundreds of samples, which is the method employed by most groups working with nanogap circuits, or we monitor continuously the tunnel current during the assembly step. We decided for the second method. The need to measure the tunnel current in real time prevented the use of assembly methods in solution, for this reason, our method is based on the projection of nanoparticles in vacuum.

3.2.1 The projection system

Our group developed a new method for trapping a single QD into a nanogap[3–5]. The principle of the method is to maintain the sample in a high vacuum box (10^{-6} mbar) and to project the QDs through a fast pulsed valve from the colloidal solution (figure 3.7). After each projection, the tunneling current between the nanogaps is measured to check for the presence of one QD within the nanogap. The cycle of projection is repeated until one QD is trapped in the nanogap, which

lead to a sharp increase of the current between the electrodes. This sharp increase of the current is detected by the measurement setup which reacts by stopping the projection system, as shown in figure 3.7. Using this method, we have fabricated junctions with different nanoparticles system, such as Au nanoparticle[3], Fe_3O_4 nanoparticle[4] and, finally, PbS QDs[5], which will be described in chapter 4.

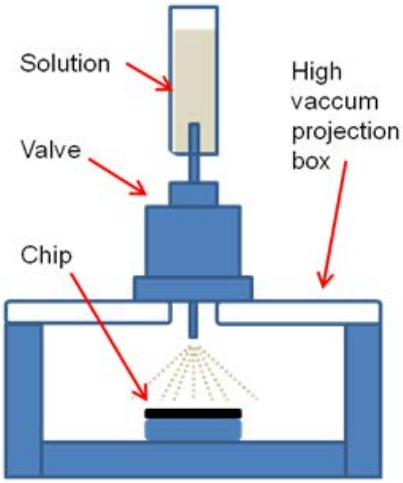

Figure 3.7: Schematic of the projection system.

3.2.2 Measurement methods

After wire bonding the chip circuit and before starting the projection, the chip is submitted to several tests of the electrical connections. Indeed, at the beginning of the chip preparation, the resistance between the drains and the source is huge, with immeasurably small currents. Consequently, it is not possible to test for a proper connection of the source and drain wires simply by measuring the current across the electrodes. However, as the gate electrode is separated from the drain and source electrodes by the insulator dielectric 300 nm thick, a capacitance of

a few picofarad can be easily measured between the electrodes and the gate. We use this capacitive coupling to test whether the electrodes are properly connected. Other tests include measures of the amount of leaking current between the drain electrodes and the gate, the source and the gate, and finally between the drain and the source.

As there are many connections and to avoid mistakes on this repetitive process, the setup has been automatized as much as possible using a scanner card and a matrix card controlled by a Labview program. The sketch of the electronic circuit is shown figure 3.8 a and a screen view of the Labview program is shown figure 3.8 b.

On this sketch, one can see that the 32 drain electrodes are connected to a scanner which provide one output, thus, this output is connected to one or more of the drain electrodes through the scanner. This output of the scanner is then connected to a matrix card, together with the source and the gate electrode. On this matrix card are also connected several instruments (Keithley 2400, lock-in, current amplifier). The connections of the matrix card are controlled digitally with the Labview program. The matrix card connects the instruments to the chip electrodes.

To test the chip circuit, five Labview sequences are run. Each sequence changes the connections of the matrix card.

These sequences are :

(1) Measure of the current between the source and the gate. A voltage up to 2 V is applied on the gate, the chip is discarded if a current more than 1 micro A is measured on the source electrode.

(2) Testing of proper wire connection on the source. An AC oscillation (1 kHz

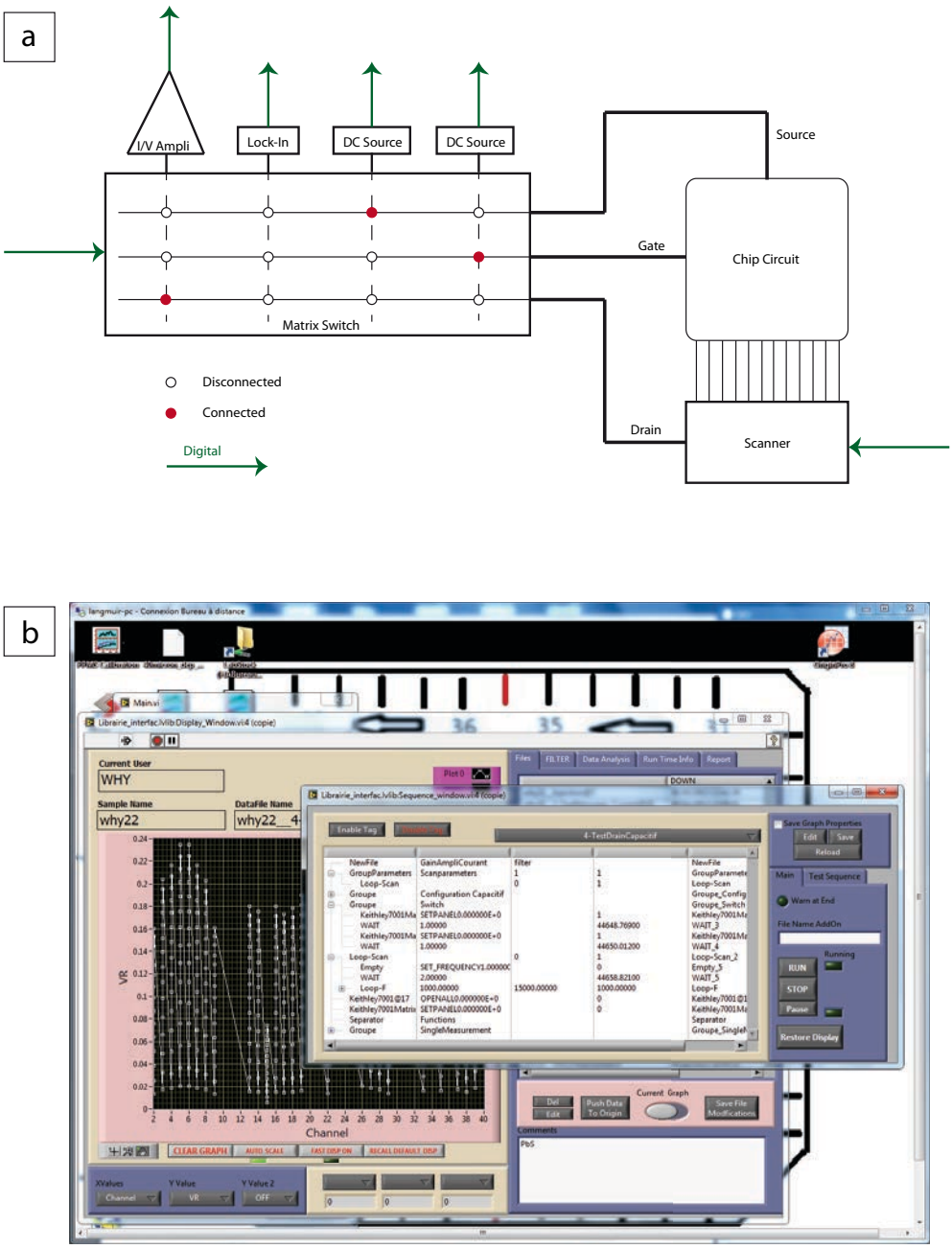

Figure 3.8: (a) Schematic of electronic measurement circuit. (b) Screen capture of the Labview program.

to 15 kHz) is applied to the gate. The current is measured on the source electrode. For a good connection, the current should change with frequency and reaches a maximum of 100 nA. If the source is disconnected, no current is measured.

(3) Testing of current leaks with the drain electrodes. A gate voltage of 1 V is applied. A source voltage from -1 V to +1 V is applied on the source. The current is measured for every drain electrodes. Drain electrodes shortened with the source are opened by electromigration. Drain electrodes shortened with the gates are removed of the list of valid electrodes and are left disconnected from the scanner during subsequent measurements.

(4) Test of proper bonding of the drain electrodes. An AC voltage (1 kHz to 15 kHz) is applied on the gate to measure the capacitance between the gate and the drain electrodes. Disconnected wires are left disconnected from the scanner during subsequent measurements.

(5) Finally, a full IV curve, from -1 V to +1 V, is measured for each drain electrode. The current should not be larger than 1 pA at the highest voltage. 1 pA is noise level of the setup. If the current is large, the electrode is left disconnected from the scanner in subsequent measurements.

Just after the tests sequences, the projection is started. The fast pulsed valve is opened for a short period (10 ms) to deposit the QDs on the chip. After a delay of 1 min required to pump the residual solvent introduced into the chamber, the current across all nanogaps is measured. This cycle, shown figure 3.9 a, is repeated until the current reaches a value above the predefined threshold of the order of 10 pA. Usually, after trapping a QD within a nanogap, the current reaches values of 1 nA or more, as shown in figure 3.9 b.

The SEM images of projected QDs on the chip are shown in figure 3.10, one

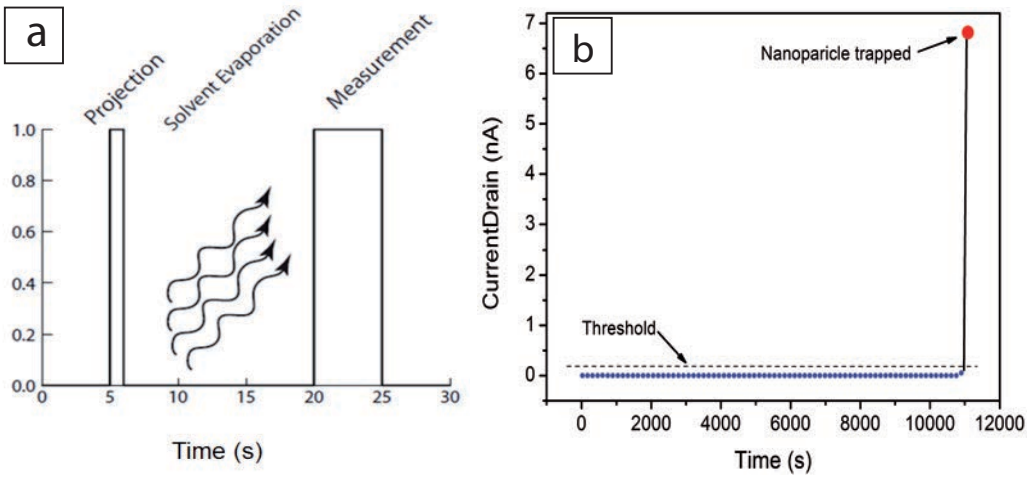

Figure 3.9: (a) The schematic of projection cycle. (b) The projection curve: the drains current as function of time.

can see that the HgTe and PbS QDs are well mono-dispersed on silicon wafer. This projection method has significant advantages. First, because the sample is fabricated in high vacuum, the tunneling current can be measured during the projection of the nanoparticles. Second, the method allows hundreds of trials, i.e. projection-measure, in a few hours, which increase significantly the probability of fabricating single nanoparticle devices.

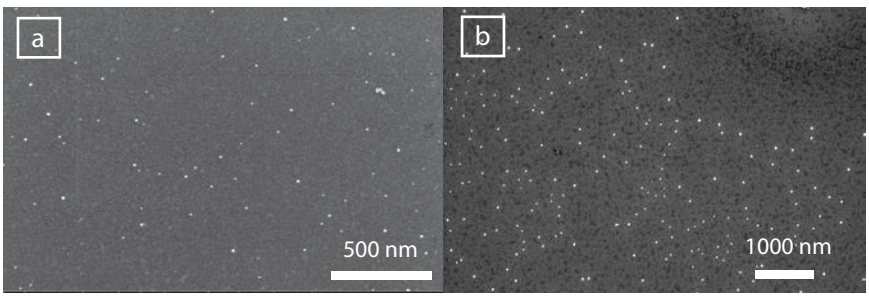

Figure 3.10: (a) The SEM image of deposited HgTe QDs. (b) The SEM image of deposited PbS QDs.

3.2.3 The electrospray ionization system

To improve the projection system based on the fast pulsed valve described above, we developed another system based on an electrospray technique. This Electro-Spray Ionization (ESI) system has been used to fabricate HgSe QDs junctions, as described in chapter 5. The ESI system has been originally developed to obtain charged molecular beams for mass spectrometry applications[6–10]. John Bennett Fenn and Koichi Tanaka have been awarded the Nobel Prize in chemistry in 2002 for their contribution to the development of electrospray ionization for large molecules in mass spectrometry applications[6]. A description of the deposition process follows[8, 9]: (1) The analyte solution is charged by the application of a high voltage ($\sim$ 3 KV) on the injector needle. (2) At the output of the injector needle, a spray of charged droplets is formed as a consequence of Coulomb repulsion. (3) As the beam of charged droplets goes through a series of vacuum chambers of decreasing pressure, the volume of the droplets decrease as the solvent evaporates. As the volume of the droplet decreases, the Coulomb energy increases in the droplet because the number of charges remains constant in the droplet as it evaporates. When the charge-to-volume ratio of the charged droplet arrives at the Rayleigh limit, the Rayleigh limit is the upper limit for the charge density on a droplet, a local deformation at the droplet surface turn into a protrusion from which a small jet of offspring droplet leaves the original parent droplet. (4) As the size of offspring charged droplets is reduced until no solvent is left, the naked charged analyte molecules are left and form a beam that is directed against a substrate. The ESI process is shown in figure 3.11 c.

To form the stable charged droplets spray, an onset voltage is required for the

injector needle[8], equation 3.1, where V_{on} is the onset voltage, γ is the surface tension of the solvent, r_c is the needle radius, and d is the distance between needle tip and counter electrode (figure 3.11 c). The smallest onset voltage is usually looked for. The equation 3.2 gives the radius R of the charged droplets coming out of the needle[8], where ρ is the density of solution, V_f is the volume flow rate, and γ is the surface tension of the solvent. From equation 3.2, a low flow rate leads to small droplets, which is the optimum ESI condition for deposition of analyte molecules or QDs.

$$V_{on} \sim 2 \times 10^5 (\gamma r_c)^{1/2} \ln(4d/r_c) \tag{3.1}$$

$$R \propto (\rho V_f^2 \gamma)^{1/3} \tag{3.2}$$

The ESI technique has been employed to depose large biomolecules[11, 6], polymers[12, 13], metal-organic complex[14–16], nano-tube[17] and nanoparticles[11] in several types of experimental studies, e.g., STM[18–20], photoemission[21] and optical spectroscopy[22–26].

The ESI technique has been successfully combined with the projection system to fabricate single QD junction on-chip in our group. As for the previous projection system, the tunneling current is monitored to check for the trapping of a single QD into the nanogaps during the ESI deposition process.

The ESI based deposition system is composed of two parts (figure 3.11 a). The first part of the ESI system is an UHV4, ultra-high vacuum compatible, electrospray deposition system, from MolecularSpray Ltd. This part of the ESI system contains three chambers with pressure about 1.2×10^1 mbar, 3×10^0

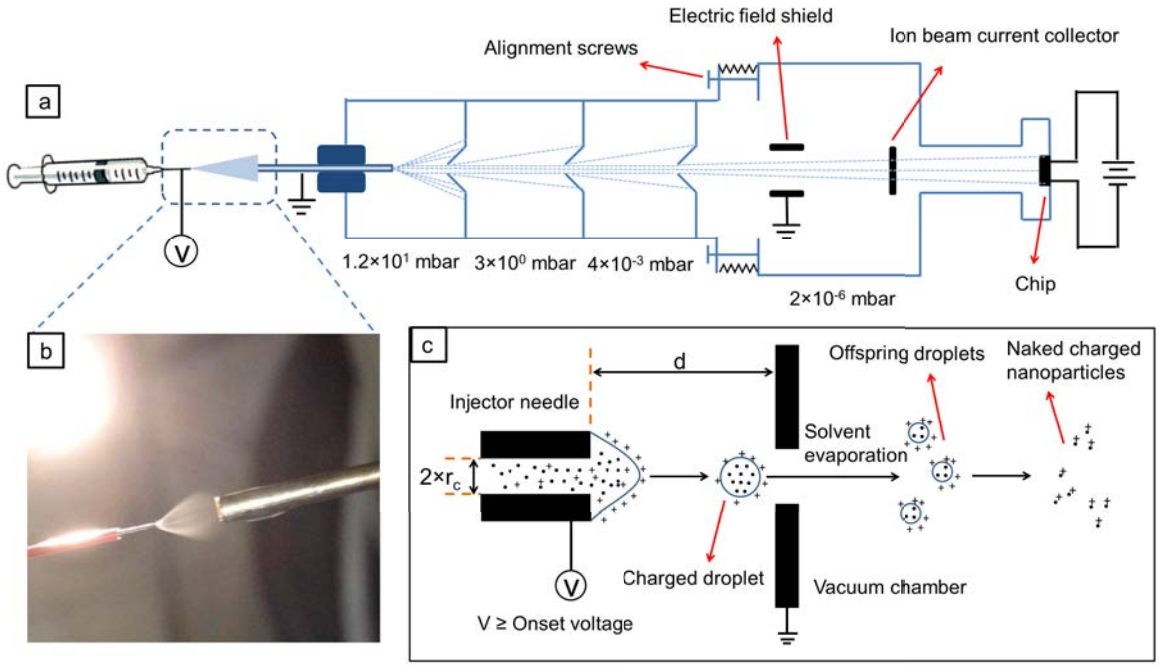

Figure 3.11: (a) The schematic of electrospray system. (b) The image of spray on a high voltage needle. (c) The evolution of charged droplets during electrospray deposition.

mbar and 4×10^{-3} mbar during the deposition, respectively. The second part of the ESI system is a large UHV chamber (2×10^{-6} mbar)in which is installed two pairs of shields used to control the vertical and horizontal positions of the beam by applying a voltage on these shields. The chamber also contains an ion beam current collector and a sample holder. The shields are useful not only to control precisely the position of the nanoparticles beam but also for filtering the beam. By applying a voltage on the shield, uncharged solvent droplets will not be deflected by the shields. However, small charged molecules, such as unbound ligands molecules, will be deflected very far off the chip. Finally, the charged nanoparticles will be only slightly displaced by the electric field. In practice,

we apply the required voltage to locate the nanoparticle beam in the center of the chip. The ion beam current collector is a simple metallic plate connected to a current-voltage amplifier. When the nanoparticle beam hits this collector, a current is measured. This current collector is used to check for the presence of the beam and to align it. The sample holder is separated from the main chamber by two gate valves, which allows (dis)connecting the sample chamber without breaking the vacuum in the main chamber and the sample chamber. After a nanoparticle is detected within a nanogap, the two gate valves are closed, the sample chamber is disconnected and transferred into the glove box. The sample chamber is then open in the nitrogen environment of the glove box, the chip is removed from his holder and inserted into a similar holder on the cryostat in the glove box. The main advantage of the ESI system with respect to the pulsed valve setup is a large reduction in the amount of solvent that is being projected on the chip circuit. As most of the excess organic ligands are contained in the solvent, reducing this solvent projection on the chip allows obtaining cleaner samples. Figure 3.12 shows the SEM images of CdSe QDs deposited on the silicon wafer by the ESI system. The QDs are well dispersed and no 'dirt' is observed around the QDs.

3.2.4 Cryostat measurement setup

After the projection step and trapping of the QD in the nanogap, the chip is transferred into the cryostat installed in the glove box. The cryostat is a closed cycle cryocooler from Advanced Research System, Inc, its base temperature is about 5 K. The cold head of the cryostat comes out in the glove box. After

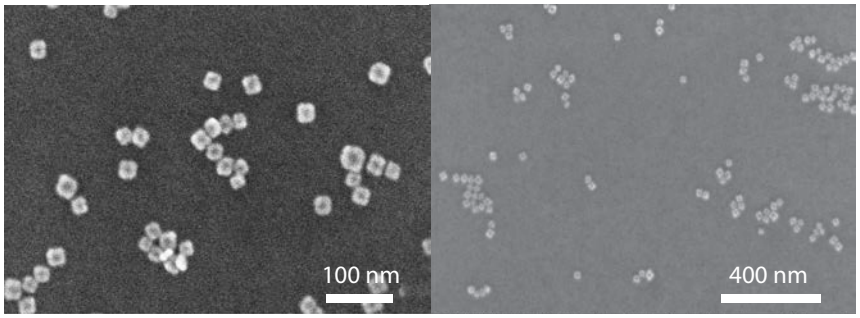

Figure 3.12: The SEM images of CdSe QDs deposited on silicon wafer.

inserting the sample, the cryostat is sealed with a shield and pumped down to low pressure (10^{-7} mbar). For photocurrent measurements, we use a shield fitted with a window.

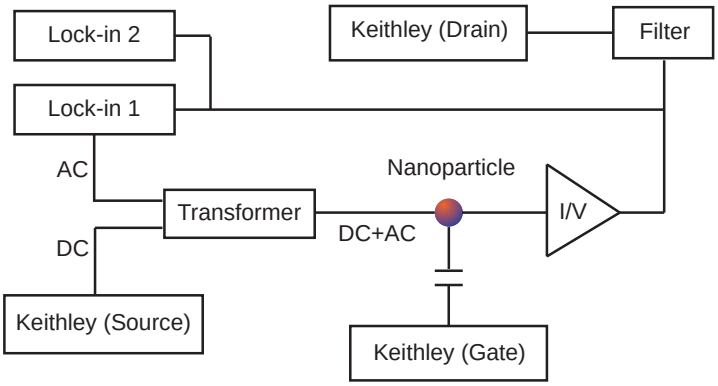

Figure 3.13: The circuit of measurement system.

The schematic of measurement circuit is shown in figure 3.13, a Keithley and a Lock-in amplifier are the source of DC and AC voltages, respectively. The DC and AC voltages are combined together with a transformer. Another Keithley is used to apply the gate voltage. The drain electrode is connected to a current to voltage amplifier (Femto), the output is read by a Keithley. The first harmonic

signal (dI/dV) and the second harmonic signal (d^2I/dV^2) are measured by the Lock-in amplifier 1 and the Lock-in amplifier 2, respectively.

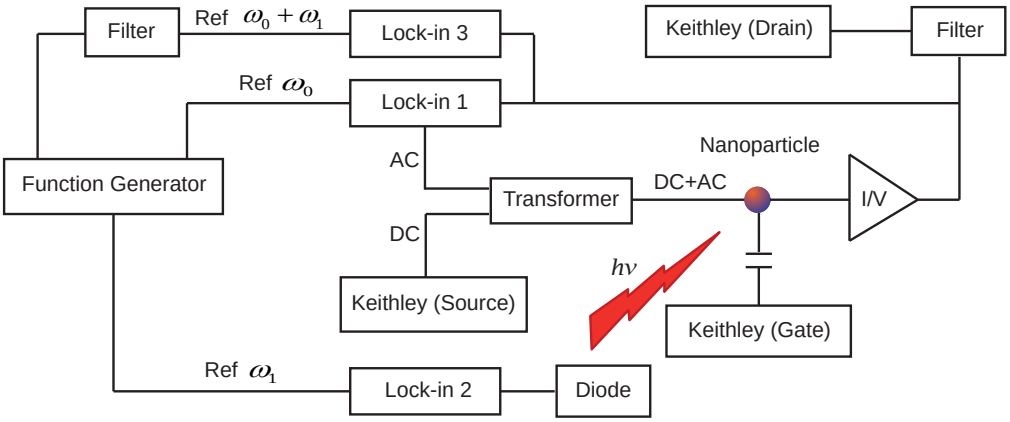

Figure 3.14: The circuit of photocurrent measurement system.

To measure the photocurrent of a single HgSe QD, we designed a new setup. Indeed, measuring the photocurrent directly with the above setup was very difficult as the photocurrent is only a small fraction of the direct tunnel current. To discriminate the photocurrent from the direct tunnel current, we designed another setup where not only the drain voltage is modulated at the frequency ω_0 but the light power is also modulated at the frequency ω_1, then, the photocurrent is measured at the frequency $\omega_0 + \omega_1$. The details of circuits are shown figure 3.14. Three reference signals ($\omega_0 = 17$ Hz, $\omega_1 = 52$ Hz and $\omega_0 + \omega_1 = 69$ Hz) are generated by a function generator. The Lock-in amplifiers 1 and 2 are synchronized to the signals ω_0 and ω_1, and are connected to the source electrode and the LED diode, respectively. The Lock-in amplifier 1 is used to measure dI/dV, using the ω_0 signal as the reference frequency. A LED diode is installed outside the cryostat facing the window inserted in the cryostat shield. The distance between

the sample and the LED is $\sim$ 10 cm. The LED provides photons of energy $h\nu \sim$ 1.88 eV to create electron-hole pairs in HgSe QD with a modulation frequency ω_1. The photoexcited electron-hole pairs are separated by the source voltage modulated at the frequency ω_0. Consequently, the photocurrent is generated at the frequency $\omega_0 + \omega_1$, which is measured by the Lock-in amplifier 3. The reference signal $\omega_0 + \omega_1$, is obtained from the function generator.

Chapter 4

Tunneling spectroscopy of single PbS QDs

In this thesis, we decided to apply the projection system for the fabrication of single nanoparticle junction with narrow gap semiconductors. This study was possible thanks to the collaboration of B. Dubertret and E. Lhuillier who started the synthesis of narrow gap semiconductors QDs in their group. They provided the QDs and I just had to do the ligand exchange before using them. Lead chalcogenides (PbS, PbSe and PbTe...) are characterized by narrow band gap in mid-infared and small electron and hole effective masses. These QDs have possible applications in LEDs[1], solar cells[2] and field effect transistors[3]. While optical spectroscopy is usually used to characterize the properties of QDs, ETS is a more relevant characterization when the goal is to incorporate the QDs into electron conducting devices. In this work, we have studied the ETS of PbS QDs. They are characterized by strong quantum confinement and a size-tunable band gap on a wide energy range. A TEM image of the PbS QDs is shown in figure 4.1 a, the

size of cubic PbS is around 10 nm. The projection curve, i.e. the tunnel current measured as function of time, is shown figure 4.1 d. A sharp increase of the current is observed indicating that a single nanoparticle getting trapped within a nanogap is likely responsible for this increase of the current. In situations where a large number of nanoparticles are required for the current to exceed the threshold, the current is observed to increase continuously. Thus, a sharp increase of the tunnel current during the projection can be safely considered as a signature of single nanoparticle trapping[4, 5]. After projection, the SEM image, figure 4.1 b, shows that the QDs are well dispersed on the chip. At this point, it should be noticed that we usually do not make any SEM image of the sample after the projection. Because of the sensitivity of the samples to air and charging effects from the SEM electron beam, making SEM images usually damages the sample. I found that a good method to prepare the sample was to project nanoparticles on the sample for some time, check on the SEM that nanoparticles were present and well dispersed on the chip, then, re-insert the chip in the projection system to keep projecting nanoparticles until a sharp increase of the current is observed. If so, the chip is immediately inserted on the cryostat and measured at low temperature. It can take a very long time, up to two months, to measure completely the I-V characteristics of a single junction.

To summarize, from these SEM images and because the measured projection curve shows a sharp increase of the tunnel current, these is no doubt that the conducting circuit obtained are single nanoparticle junctions.

10 circuits chips have been fabricated and the ETS have been measured from T=300 K to T=5 K. In this studies of PbS QDs, three samples A, B and C are shown here, we have observed three distinct signatures of strong electron-phonon

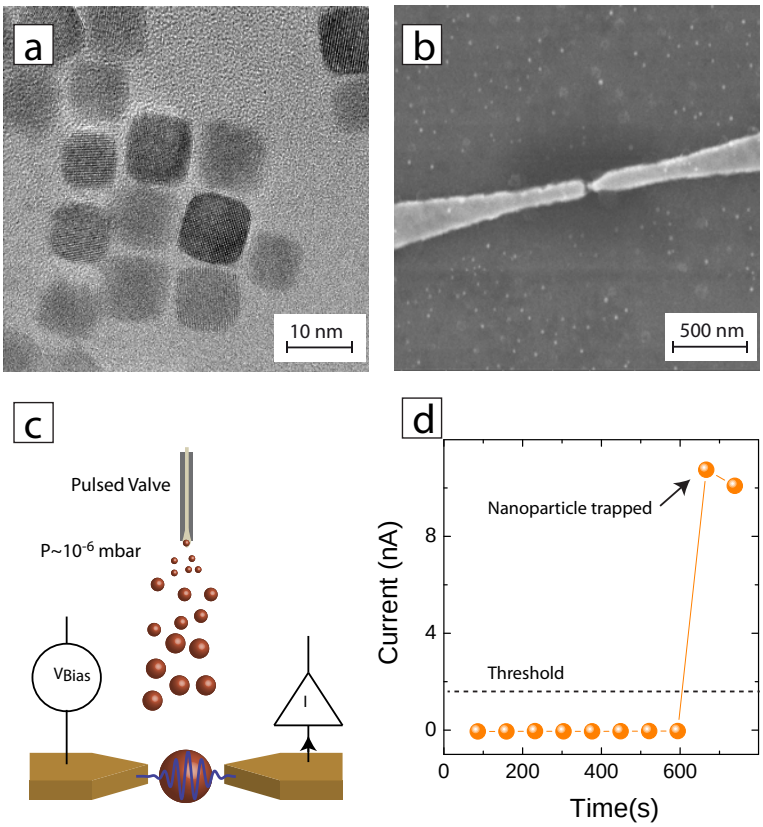

Figure 4.1: (a) The TEM image of PbS QDs.(b) The SEM image of $\sim$ 10 nm spaced electrodes in which a PbS QD has been deposited. (c) QDs are projected onto the chip-circuit in high vacuum using a fast pulsed valve. (d) After each projection, the tunneling current is measured (V_{Drain}=1 V, V_{Gate}=0 V, T=300 K). When the tunneling current is exceeds the threshold, the projection stops.

coupling in the ETS. In the shell-filling regime, the 8 times degeneracy of the electronic levels is lifted by the Coulomb interactions and allows the observation of phonon sub-bands that result from the emission of optical phonons. At low bias, a gap is observed in the ETS that cannot be closed with the gate voltage, which is a distinguishing feature of the Franck-Condon (FC) blockade. From the data, a Huang-Rhys factor in the range 1.7 to 2.5 is obtained. Finally, in the shell tunneling regime, the optical phonons appears in the inelastic ETS d^2I/dV^2.

4.1 Coulomb blockade in single PbS QDs

Figure 4.2 shows the dI/dV curves measured on sample A at two different temperatures. At the highest temperature, $T = 77$ K, the curve shows conductance peaks corresponding to the excited hole levels $1S_h$, $1P_h$ and electron level $1S_e$ of the QD. At the lower temperature, $T = 5$ K, the ETS is modulated by sharp conductance peaks which are characteristics Coulomb blockade peaks in the shell filling regime[6, 7]. In this regime, the tunneling rate Γ_{in} for electrons entering the QD is larger than the tunneling rate Γ_{out} for electrons escaping the QD. The inset of figure 4.2 shows that a single Coulomb peak has a width ~ 20 meV which is much broader than the thermal smearing at T = 5 K. Similar broadening were observed in STM spectra on CdSe[8] and PbS[9] QDs.

Because PbS has the rock salt crystal structure and, as a result, has the direct band gaps at four equivalent L points in the Brillouin zone[10, 11], the excited levels $1S_e$ and $1S_h$ are 8 times degenerated, after accounting the spin degeneracy. In the shell filling regime, this implies that such 8 peaks separated by Coulomb blockade should be observed in the conductance curve. From the voltage

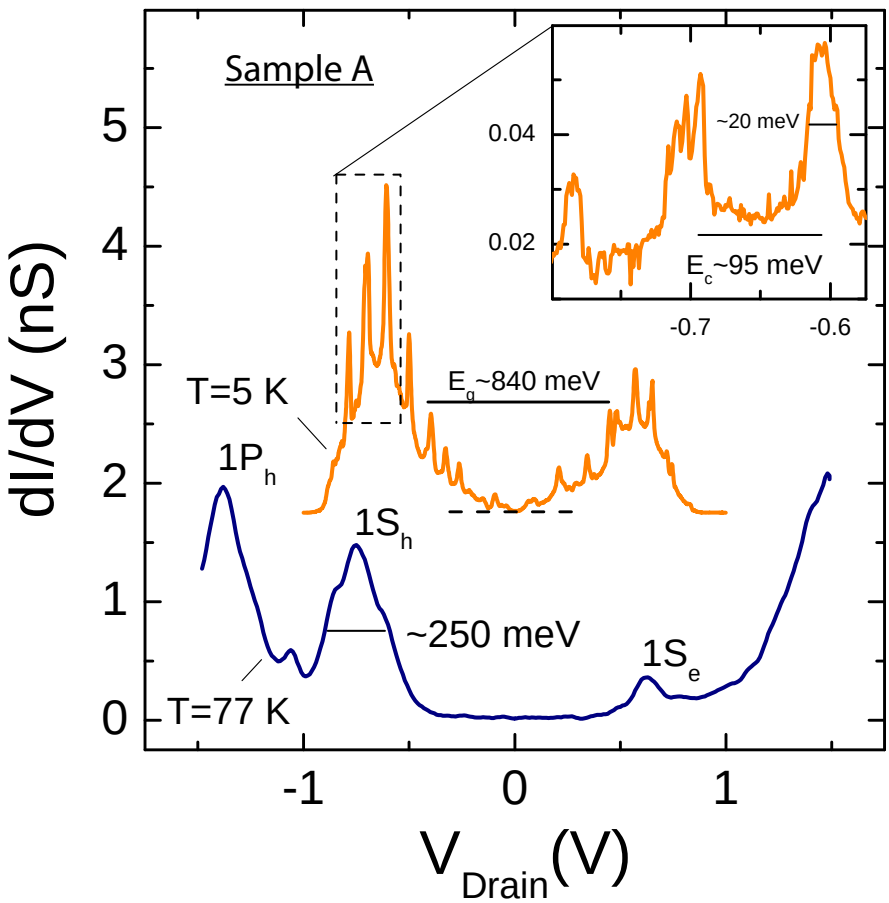

Figure 4.2: Conductance curve dI/dV for sample A. The curve at $T = 77$ K shows the main excited levels $1S_h$, $1P_h$ and $1S_e$. The curve at $T = 5$ K shows that the degeneracy of the excited levels has been lifted by the Coulomb interactions and gives rise to Coulomb peaks. This last curve has been shifted up for clarity, where the dash line indicates zero level. The inset is a zoom on the Coulomb peaks showing that their width, ~ 20 meV, is larger than thermal smearing ~ 0.45 meV. For these measurements, $V_{Gate} = 0$ V.

separation between two peaks in figure 4.2, we obtain the value E_c ~95 meV for the Coulomb energy. This experimental value is consistent with calculated Coulomb energy $E_c = e^2/2C_{self}$ where $C_{self} = r/(1/\kappa_m + 0.79/\kappa_{PbS})$ is the self-capacitance of the QD, using for the diameter $2 \times r \sim 8.5$ nm, $\kappa_m = 4\pi\varepsilon_m\varepsilon_0$ with $\varepsilon_m = 1.8$, which is the average dielectric coefficient of the media surrounding the QD, and $\kappa_{PbS} = 4\pi\varepsilon_{PbS}\varepsilon_0$ where $\varepsilon_{PbS} = 170$ is the static dielectric coefficient of PbS. This analysis ignores a possibly small contribution of the electrodes to the Coulomb energy.

$$\Sigma = 0.5\frac{e^2}{r}(\frac{1}{\kappa_m} - \frac{1}{\kappa_{PbS}}) + 0.47\frac{e^2}{\kappa_{PbS}r}\frac{\kappa_{PbS} - \kappa_m}{\kappa_{PbS} + \kappa_m} \tag{4.1}$$

From these parameters and equation 4.1, we also obtain the polarization energy[12, 13], $\Sigma \sim 95$ meV. We also extract, the tunneling gap $E_g \sim 840$ meV which is related to the excitation gap E_{g0} through the relation $E_g = E_{g0} + 2\Sigma$, which allows extracting the excitation gap $E_{g0} \sim 640$ meV at 5 K. This value is consistent with the excitation gap expected from **k.p.** four bands envelope function formalism[10].

Figure 4.3 a shows the dI/dV curves for sample A as function of gate voltage, shown on the color plot figure 4.3 b. At any gate voltage, exactly 8 Coulomb peaks can be clearly observed as function of drain voltage. This implies that the injected electrons are indeed populating the $1S_e$ and $1S_h$ levels of the QD. The fact that excitation occur primarily in one direction is due to asymmetric tunnel barriers[14]. This behavior can be simulated with the SIMON simulator. This software has been designed by C. Wasshuber and allows simple simulations of Coulomb blockade in QDs.

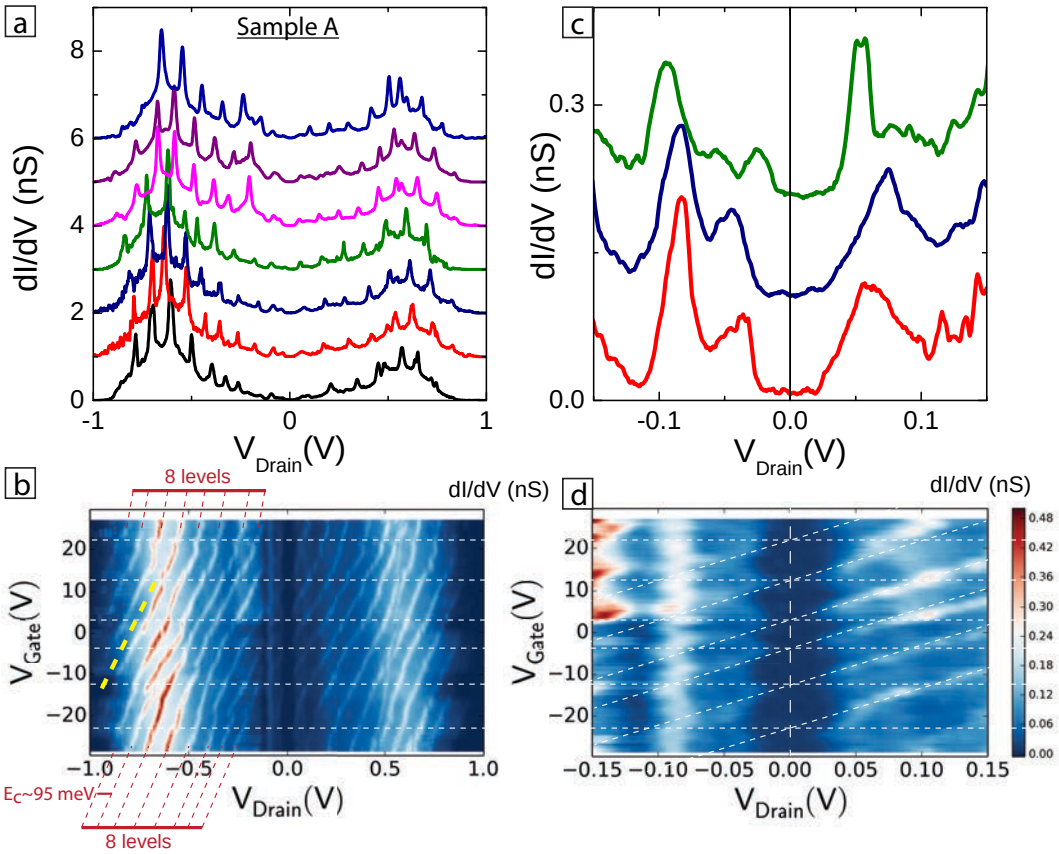

Figure 4.3: (a) dI/dV curves for sample A at V_{Gate} = -27, -17, -7, 0, 7, 17, 27 V (from bottom to top).(b) The color plot of dI/dV as function of drain and gate voltage at 5 K. The red dashed lines are used to highlight the eight Coulomb peaks of the $1S_h$ excited level. The yellow dashed line is used to calculate the back-gate lever arm α_C. (c) The zoom on the dI/dV curves at low bias from V_{Drain} = -0.15 V to V_{Drain} = 0.15 V for V_{Gate} = -17, -7, 0 V (from bottom to top). (d) The zoom of the color plot (a) from V_{Drain} = -0.15 V to V_{Drain} = 0.15 V. The white horizontal dashed lines highlight the gate voltage where the number of electrons in the QD is changed by one. This zoom shows that the gap at low bias cannot be lifted by the gate voltage. On panels a) and c), the curves have been shifted up for clarity.

In the simulation, we defined the QD as a system with one electron level (7 times degenerated) and one hole level (three times degenerated). The QD is separated from the Drain (electrode 1) and Source (electrode 2) by two tunnel barriers, J1 and J2, which are characterized by their resistances, (R1, R2) and their capacitances (C1,C2). Furthermore, a gate electrode is included in the simulation, characterized by a gate capacitance C_{gate}. The lever arm $\eta_{1(2)}$ for the electrode 1(2) depends on the capacitance through the relation $\eta_{1(2)} = 1 - C_{1(2)}/\sum C$.

For a symmetric junction with identical tunnel barriers, the electronic spectrum should also be symmetric with respect to the axe $V_{Drain} = 0$, as observed on the simulated spectrum figure 4.4 a. On the positive side, the electron (hole) levels are labeled e^+ (h^+), on the negative side, the electron levels are labeled e^- (h^-). Upon increasing the gate voltage, the electron and hole levels evolve symmetrically with respect to the Drain bias, as shown by the simulation figure 4.4 a and the sketch figure 4.4 c. Upon increasing the capacitance of one of the junctions, the spectrum becomes non-symmetric with respect to $V_{Drain} = 0$. Indeed, as the lever arm changes from $\eta = 0.5$, an electronic level will be observed at different $|V_{Drain}|$ voltages on both sides of the spectrum. In highly asymmetric junctions such as in STM experiments, electron type levels are only seen on one side of the spectrum, while hole type levels are observed on the other side, as shown figure 4.4 b.

In the STM experiment described in Ref.[15], it was shown that the nature of the electronic level, i.e. hole or electron type, could be identified by studying the evolution of the electronic levels with the lever arm. This lever arm can be changed through the height of the tip, which depends on the tunnel current

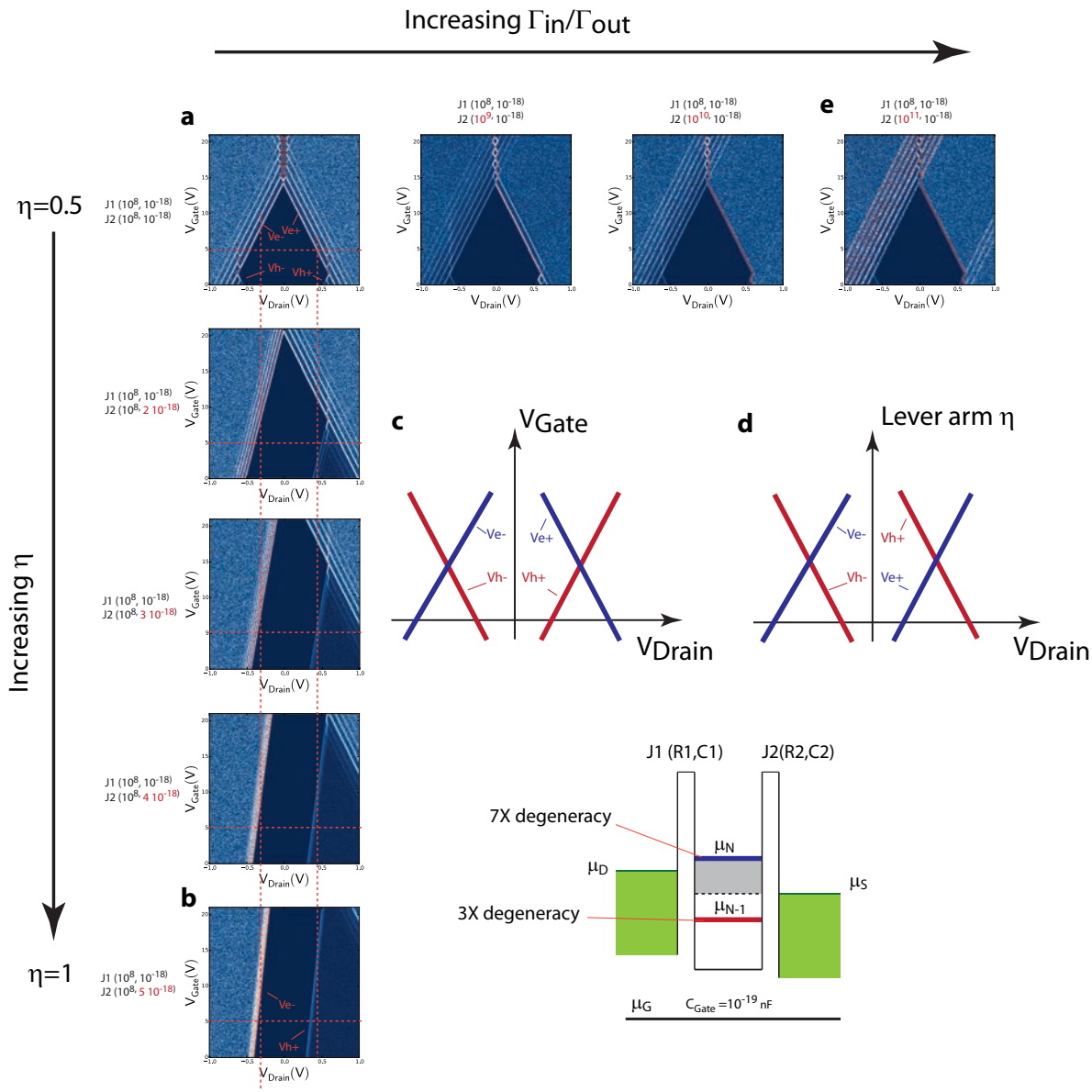

Figure 4.4: Simulation of a QD constituted of an electron level, seven times degenerated, and a hole level, three times degenerated. Panel a) Symmetric junction. In this spectrum, the electronic levels evolve symmetrically around the axis $V_{Drain} = 0$ upon increasing the gate voltage. Panels a) to b), the level arm η increases upon increasing the capacitance of the junction 2. As this level arm increases, the electron (hole) levels on the positive (negative) side are shifted to higher voltages. In the highly asymmetric junction, panel b), the electron levels are only seen on one side, while the hole levels are seen on the other side. Panels a) to e), the tunnel resistance asymmetry increases. As this asymmetry increases, the Coulomb splitting of the spectrum disappears on one side of the spectrum as the system evolves from shell filling to the shell tunneling regime.

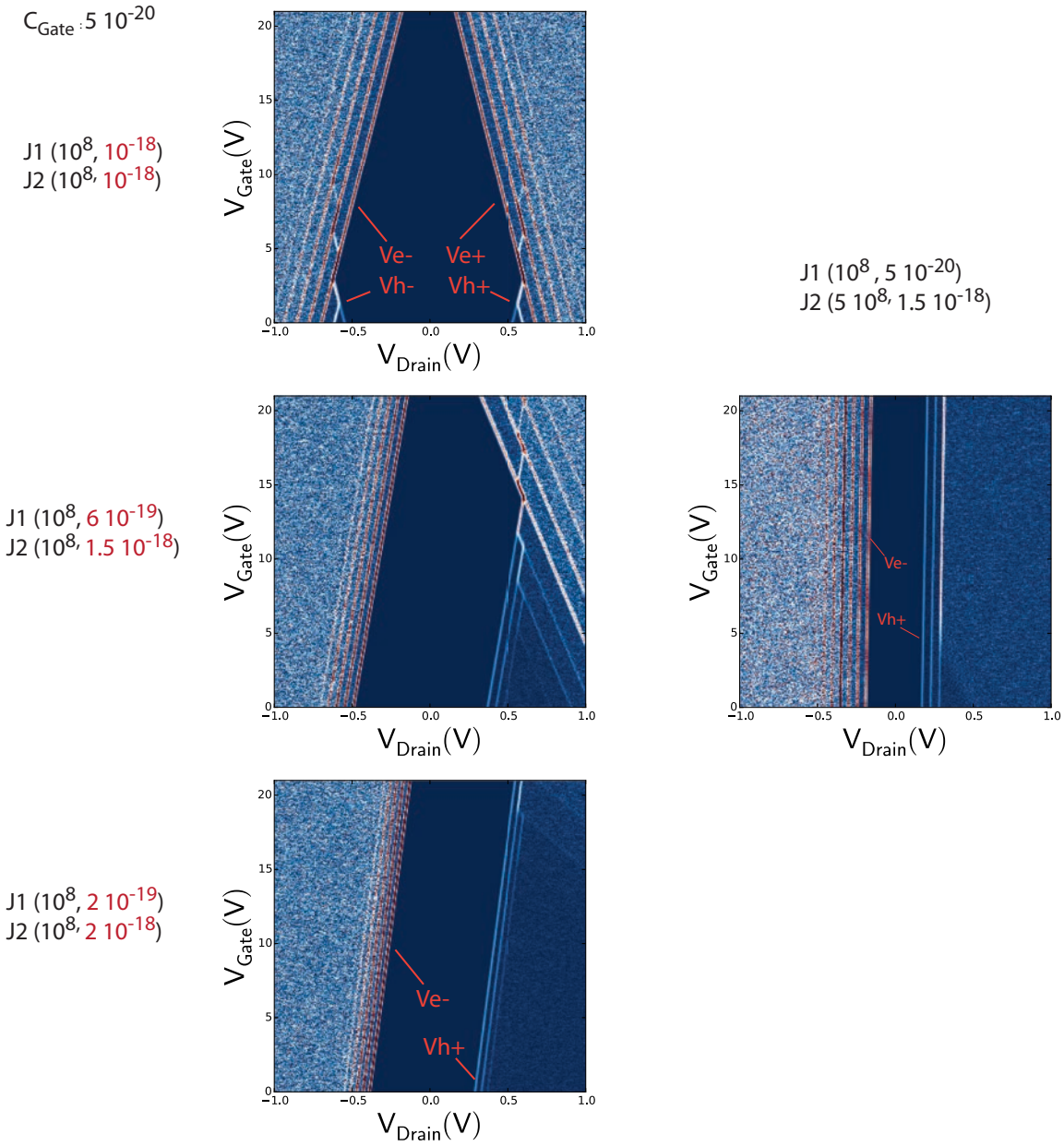

Figure 4.5: Simulation of the electronic spectrum for different values of the capacitance. For the symmetric junction, panel a), the electron and hole states are observed on both sides of the spectrum, they evolve symmetrically with respect to the axis $V_{Drain} = 0$. As the lever arm increases, the electron (hole) disappear on the positive (negative) side of the spectrum. In this last situation, the electron and hole states are parallel to each other in the $V_{Drain} - V_{Gate}$ diagram.

setpoint. It was shown that, upon changing the lever arm, the electronic levels of the same type (electron or hole) should evolve anti-symmetrically with respect to the axe $V_{Drain} = 0$, see figure 4.4 d. Thus, we see that the electronic levels evolve differently with the gate voltage and the lever arm, as sketched figure 4.4 c and figure 4.4 d.

Figure 4.5 shows the simulated electronic spectrum for different values of the capacitances of the junctions. This figure shows clearly that a large difference in the capacitance of the junction J1 and J2 leads to electron levels appearing on the negative side only and hole levels appearing on the positive side only. Upon increasing the gate voltage, the electron state approach the Fermi level of the electrodes, while the hole state go away from the Fermi level. For this reason, the electron and hole levels appearing on the opposite side of the axis $V_{Drain} = 0$ are seen to move parallel to each other in the $V_{Drain} - V_{Gate}$ diagram.

In our data, the observation of an asymmetric spectrum implies that the junction is asymmetric with a large difference between the source and drain capacitances, implying that the lever arm is close to 1.

4.2 Phonon sub-bands and Frank-Condon blockade

4.2.1 Phonon sub-bands in electron tunneling spectrum

The Coulomb diamonds are also observed for sample B, as shown in figure 4.6 b. From the experimental value of Coulomb energy $E_c \sim 50$ meV we find that the QD diameter is $2 \times r \sim 16$ nm. With this bigger diameter, the excitation

level are too broad to be clearly observed. However, as figure 4.6 a show, this sample allows the clear observation of phonon sub-bands. A zoom at the Coulomb peaks measured on sample B, figure 4.6 a, clearly shows that the Coulomb peak is constituted of sub-bands separated by an energy of $\sim$ 8 meV. These peaks can also be observed for sample A, but with lower resolution. These peaks are equally spaced and strongly resemble the expected response when the electron level is coupled to phonon modes[16–18]. This behavior has been observed previously in STM spectroscopy of CdSe QDs[8], in molecules[19–21] and nano-tubes based QDs[22, 23], as described in chapter 2.

In bulk PbS, the energy of the zero-wave-vector (Γ-point) transverse-optical phonon is 8.1 meV as observed through far-infrared absorption[24] spectroscopy and Raman spectroscopy[25, 26]. Thus, the observed side-bands are consistent with the emission of these transverse optical-phonons. Furthermore, vibronic quantum beats have also been observed in femtosecond optical spectroscopy[26, 27] of PbS QDs.

4.2.2 Frank-Condon blockade

The coupling of electronic levels with phonons can be described in terms of the Frank-Condon model[16–18]. In the case of a single phonon mode $\hbar\omega_0$, the FC theory gives for the transition probability:

$$X_{0n}^2 = | < 0|X|n > |^2 = \frac{e^{-\lambda^2}\lambda^{2n}}{n!} \tag{4.2}$$

between a state with 0 phonon and a state with n phonons where λ is the electron-phonon coupling strength, also called the Huang-Rhys factor. Figure

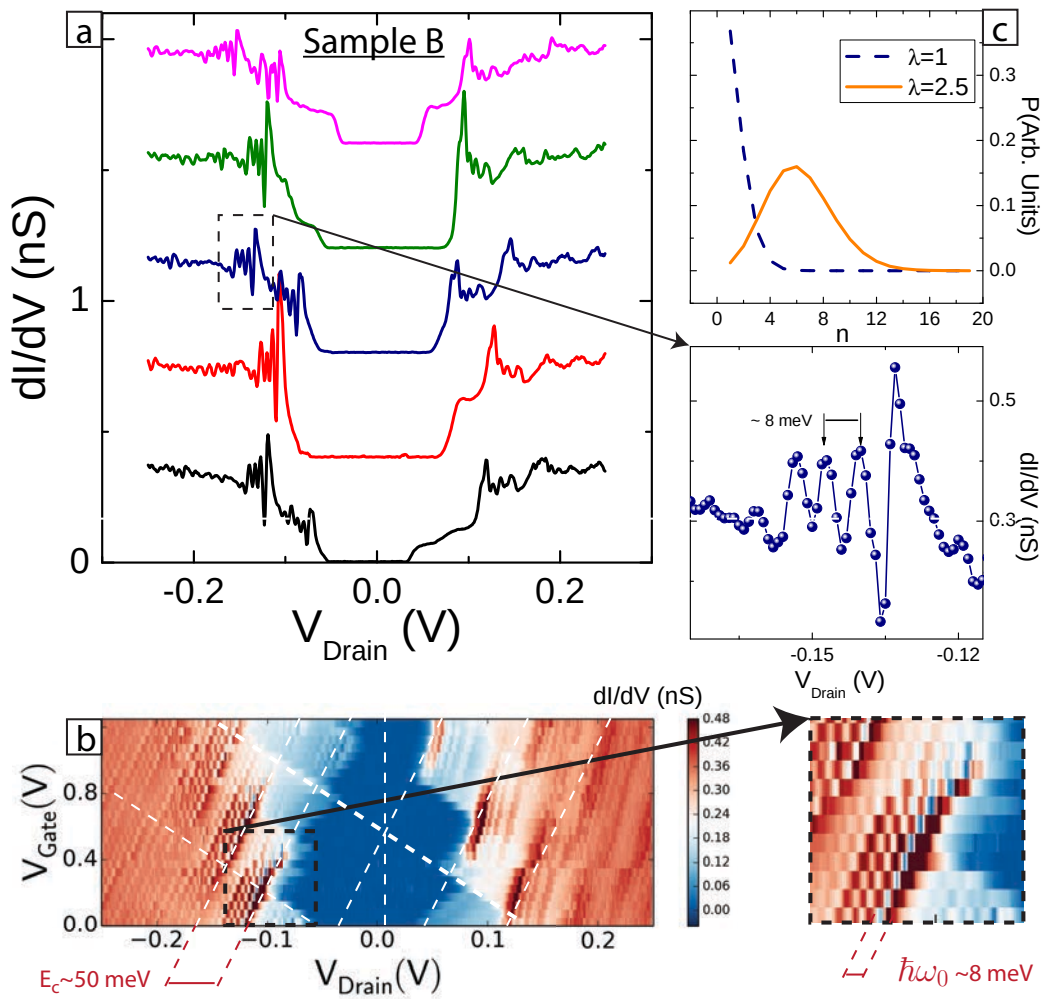

Figure 4.6: dI/dV curves for sample B, plotted on panel (a) from $V_{Gate} = 0$ V (bottom) to $V_{Gate} = 1.2$ V (top) and shown on the color plot (b) as function of drain and gate voltage, measured at 5 K. There panels show that the gap a low bias cannot be lifted by the gate voltage. The zoom on the dI/dV curve at $V_{Gate} = 0.4$ V and the zoom on the color plot show that a single Coulomb peak is formed of phonon sub-bands separated by the phonon energy $\hbar\omega_0 \sim 8$ meV. (c) Theoretical amplitude, equation 4.2, of the FC peaks as function of the number of emitted phonons for two values of the Huang-Rhys factor $\lambda = 1$ (dashed line) and $\lambda = 2.5$ (continuous line). At large λ, the matrix element goes to zero for small n, indicated the FC blockade.

4.6 c shows the tunneling probability obtained from the equation 4.2, as function of the number of emitted phonons for two values of the Huang-Rhys factor. When tunneling on the QD, the electron shifts the equilibrium coordinate of the QD by an amount proportional to the Huang-Rhys factor λ. As the overlap between states of different phonons occupation is exponentially sensitive to this geometrical displacement, the tunneling probability of ground-state to ground-state transition is exponentially suppressed for strong electron-phonon coupling as shown by the continuous line, $\lambda = 2.5$, on the figure 4.6 c. This phenomena, called Frank-Condon blockade[28, 29], could be responsible of the conductance suppression at low bias for both samples A and B, as shown figure 4.3 and figure 4.6, respectively.

While the Coulomb blockade can always be lifted at appropriate gate voltage values, the FC blockade cannot be lifted at any gate voltage because of the strong electron-phonon coupling, as shown figure 4.6 and figure 4.7, which is a distinguished feature of the FC blockade. The first observation of FC blockade in a tunneling experiment has been observed on carbon nano-tube based QDs[22, 23] where the electrons were coupled to vibration modes (vibrons) of the nano-tube.

For equilibrated phonons, this suppression dominates until the bias voltage is high enough, $eV \sim \lambda^2\hbar\omega_0$[28, 29], to escape from the FC blockade regime by transitions from zero phonons to highly excited phonon states. From the observed gap values for sample A ($\sim$ 25 meV) and sample B ($\sim$ 50 meV), we find that the electron-phonon coupling constant is in the range $\lambda \sim 1.7 - 2.5$, which is very large, of the order of the Huang-Rhys factor obtained from Raman scattering experiments[25]. While there is no consensus on the effects of quantum confinement on electron-phonon coupling, see. Ref. [30] for a review, it has been

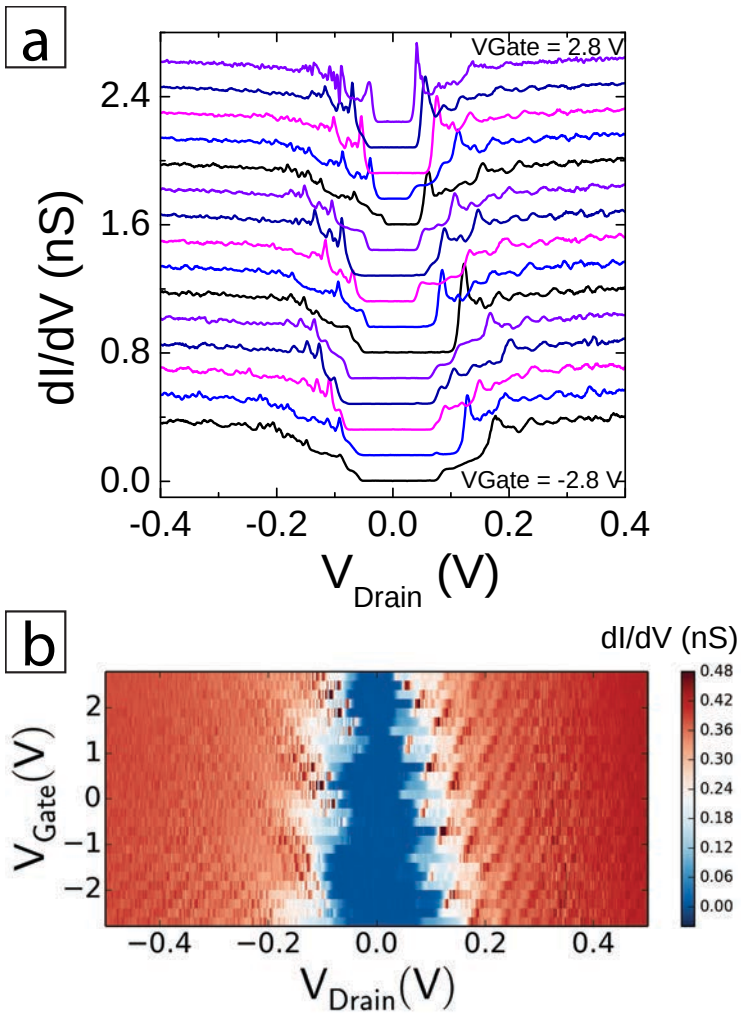

Figure 4.7: dI/dV curves for sample B, plotted on panel (a) from V_{Gate} = -2.8 V (bottom) to V_{Gate} = 2.8 V (top) and shown on the color plot (b) as function of drain and gate voltage, measured at 5 K. There panels show that the gap at low bias cannot be lifted by the gate voltage.

suggested that a large electron-phonon coupling in QDs could be the consequence of trapped charges at the surface of QDs[25] or polaronic effects that would arise as a consequence of the discrete electronic levels[31].

4.3 Inelastic tunneling spectroscopy of PbS QDs

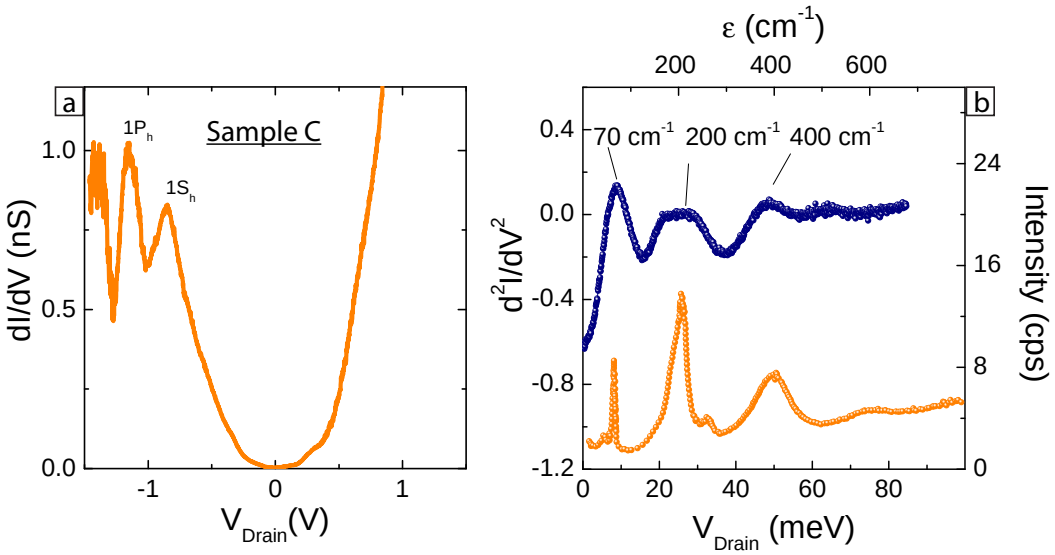

Figure 4.8: (a) dI/dV curve for sample C showing the excited hole levels, $1S_h$ and $1P_h$, at 5 K. Note the absence of the Coulomb peaks in this shell-tunneling regime.(b) Inelastic ETS d^2I/dV^2 showing three lowest phonons mode (blue line) compared to the Raman spectrum (yellow line) extracted from Ref[25].

Phonon modes can also be observed in the inelastic ETS[32], as shown in figure 4.8 b for sample C which is in the regime of shell-tunneling[7, 6], In this regime, the tunneling rate Γ_{in} for electrons entering the QD is smaller than the tunneling rate Γ_{out} for electrons escaping the QD, and, consequently, do not present Coulomb peaks, as shown figure 4.8 a. The absence of the sharp Coulomb blockade peaks does not allow the observation of phonon sub-bands, however, the absence of the

gap at low bias allows measurements of the inelastic ETS (d^2I/dV^2), as shown in figure 4.8 b. This spectrum shows the first three optical phonon modes (blue line) at the position expected from Raman spectroscopy (yellow line)[25]. The energy of the first phonon mode is around 8 meV which is the energy of phonons extracted from the phonon sub-bands in sample B.

4.4 Capacitive coupling between the gate and QDs

In this section, we return to the sample A and B. Using the formula for the capacitance between a metallic sphere of radius r and a metallic plane at a distance d:

$$C = \sum_{n=1}^{+\infty} \frac{\log(d/r + \sqrt{(d/r)^2 - 1})}{\sin h(n \log(d/r + \sqrt{(d/r)^2 - 1}))} \tag{4.3}$$

We calculate the capacitance between the QD of radius r and the gate at the distance d =300 nm, which gives C_{sp}/e =5.3 V^{-1} for sample A and C_{sp}/e =10.2 V^{-1} for sample B. We find for the experimental values C/e =0.1 V^{-1} for sample A and C/e =2.5 V^{-1} for sample B. These values are smaller than the theoretical values because of the screening effects due to the electrodes, which depend on the exact position of the QD with respect to the electrodes. One can see, for sample A, that the back-gate lever arm is different for the Coulomb peaks and the excited levels ($1S_e, 1S_h$). While the lever arm for the Coulomb peak is $\alpha_C = dE_c/dV_{Gate}$ $\sim$ 0.0085, it seems that the excitation peaks are barely shifting with the gate. This can be understood as a consequence of the good screening properties of PbS

which has a large static dielectric coefficient.

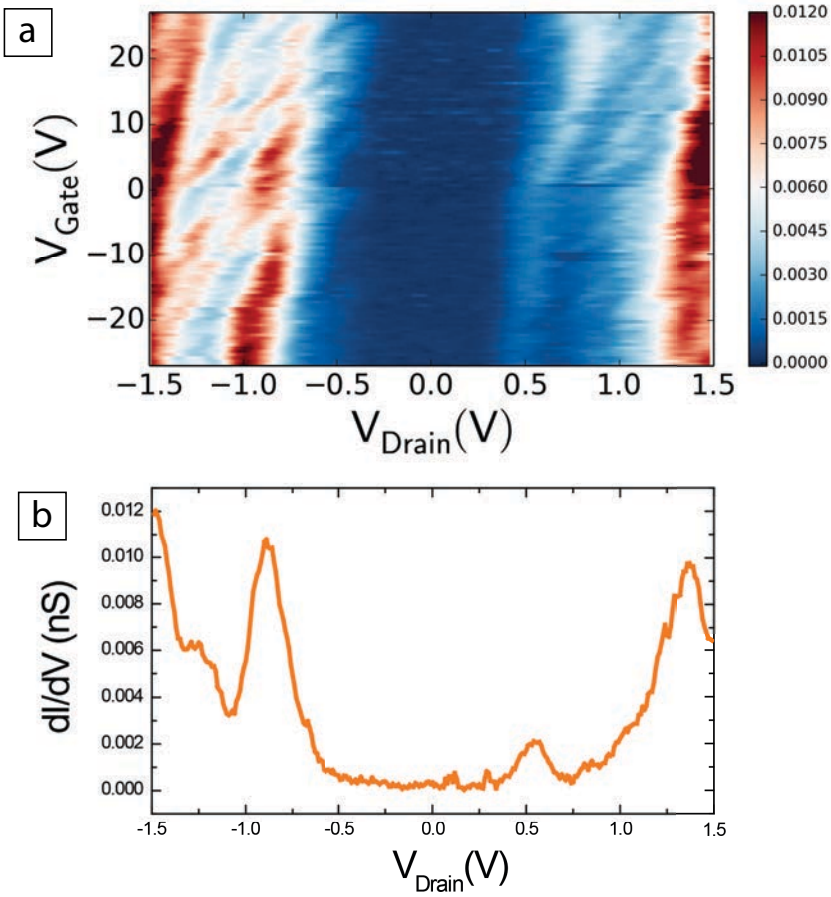

Figure 4.9: (a) Color plot of the differential conductance for sample A measured at the temperature $T = 77\ K$, as function of drain and gate voltages. This plot shows the splitting of the excitation level with the gate voltage. (b) Differential conductance as function of drain voltage extracted from the color plot at $V_{Gate} = 0\ V$.

However, measuring the differential conductance map at higher temperature, T=80K, shown figure 4.9, one can see that the excited levels 1S and 1P are actually shifting and splitting with the gate voltage. We believe that this observation is possible at 80 K and not 5K because of the absence of the Coulomb peaks

at the higher temperature. The origin of the splitting is not completely clear. Because the amplitude of this splitting is very large, $\sim 100meV$, it cannot be due to a Starck effect. One plausible explanation is that this phenomena is related to a screening effect. As seen for large microfabricated QDs, the accumulation of charges in a QD leads to a gate voltage dependent screening length, and so, to a gate dependent Coulomb blockade. In semiconductors, the screening length is actually related to the Debye length, which provides a measure of the band bending in the semiconductor in presence of an electric field. In the case of PbS, because the bands are four times degenerated, the amplitude of band bending could be different for each bands as they are corresponding to different crystallographic orientation, and so, they are oriented differently with respect to the applied electric field. Thus, the observed splitting of the excited peak in the color plot shown figure 4.9 could be related to the lifting of the four-fold degeneracy of the excited level.

A final remark regarding the observation of Coulomb diamonds is in order. Indeed, the observation of Coulomb diamonds is usually expected in metallic nanoparticles or in semiconducting QDs where the Fermi level has been driven in the conductance or valence band with the gate voltage. At T=5 K, we see that the applied gate voltage is not sufficient to push the excited levels across zero bias, however, the broadening of excited levels is sufficient to produce a residual density of states within the semiconducting gap, allowing the QD to effectively behave as a metallic nanoparticle. This is consistent with the recent STM observation of mid gap states in PbS QDs[9] and transport measurements in PbS QDs thin films[33].

4.5 Conclusion

To summarize, we found that the elastic and inelastic ETS of PbS QDs is characterized by signatures of strong electron-phonon coupling. In the shell-tunneling regime, three phonon modes can be observed in the *inelastic* ETS d^2I/dV^2. In the shell-filling regime, where the Coulomb blockade peaks are observed, the lowest energy phonon mode leads to the apparition of sub-bands that can be observed in the *elastic* ETS dI/dV. In this regime, we observe that the Coulomb blockade cannot be lifted at any gate voltage, which is likely the consequence of FC blockade. Thus, this first report of the observation of FC blockade induced by coupling of electrons to optical phonons teaches us that using QDs with weak electron-phonon coupling should help improve electronic transport in QDs thin films.

Chapter 5

Tunneling spectroscopy of single HgSe QDs

As described in chapter 2, HgSe has an inverted band structure, with the s-like Γ_6 level below the Γ_8 and the Γ_7 levels, where the Fermi level is located on the Γ_8 level. The consequence of quantum confinement in those inverted band structure is two-fold. On the one hand, the position of the Γ_6 level increases in the band structure. Below some critical radius, the Γ_6 level should becomes higher than the Γ_8 level. In HgTe, a critical radius $r = 9$ nm has been calculated[1]. At this point, we are not aware of any similar calcuations for HgSe, and we do not know what should be the critical radius for HgSe. On the other hand, quantum confinement leads, of course, to the apparition of discrete levels in the valence and conduction band, separated of a few hundreds meV. This band structure is of interest for application in Infra-Red Detectors[2–4], which can make use of either interband[5–7] or intraband transitions[3, 8].

The interband transition and the intraband transition of HgSe QDs have been

studied by optical characterization[3, 8], however, as already discussed in the chapter 4 on PbS, electron tunneling spectroscopy is a more relevant characterization when the goal is to fabricate QDs-based electron-conducting devices. Using the ESI technique, which is described in the chapter 3, we fabricated single HgSe QD junctions.

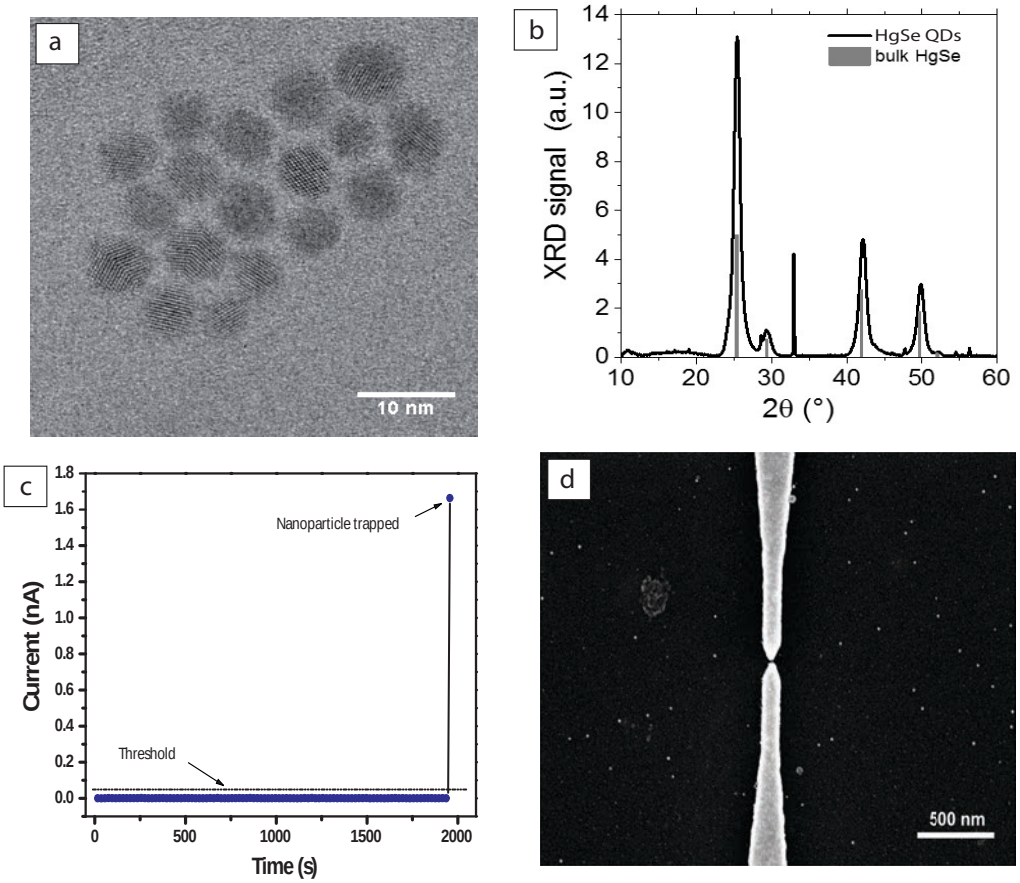

Figure 5.1: (a) TEM image of HgSe QDs. (b) The XRD diffraction curve of HgSe. (c) After each projection, the tunnel current is measured ($V_{Drain} = 0.5$ V, $V_{Gate} = 0$ V, T=300 K). When it exceeds the threshold, the projection is stopped. (d) SEM image of ~ 10 nm spaced electrodes in which a QD has been deposited.

Figure 5.1 a shows that the HgSe QDs are sphere of size $\sim$ 10 nm in diameter,

well crystallized as shown by the XRD spectrum, figure 5.1 b. The QDs are deposited on the chip circuit with the ESI system until a sharp increases of the tunnel current is observed, as shown in figure 5.2 c. After a typical deposition, figure 5.1 d shows that the HgSe QDs are well dispersed on the chip. We have successfully fabricated several HgSe QD junction circuits with the ESI techniques and the ETS of HgSe QD junction are measured at the temperature T $\sim$ 80 K.

5.1 The interband and intraband transition of HgSe QD

Figure 5.2 b shows a sketch of the main electronic levels in the QD. The electron transition from $1S_h$ to $1S_e$ is called interband transition and the electron transition from $1S_e$ to $1P_e$ is called intraband transition. Both of these two transitions have been observed by optical absroption (figure 5.2 a) by E. Lhuillier et al., our collaborator who provided the HgSe samples.

Figure 5.3 shows the conductance spectrum dI/dV as function of gate voltage for two samples, A and B. Overall, the differential conductance maps are found to be similar for both samples. These maps present distinct regimes according to the carrier filling. At the most negative voltage, in the regime labeled I, the conductance map shows a large gap of amplitude about $\sim$ 1.8 V. At the highest voltage, regime labeled IV, the conductance map shows a smaller gap about $\sim$ 0.4 V. Assuming that the voltage drop across one junction corresponds to one half of the applied voltage, as expected for a symmetric junction, the measured gaps corresponds respectively to the interband gap, $\sim$ 0.8 eV, and the intra-band

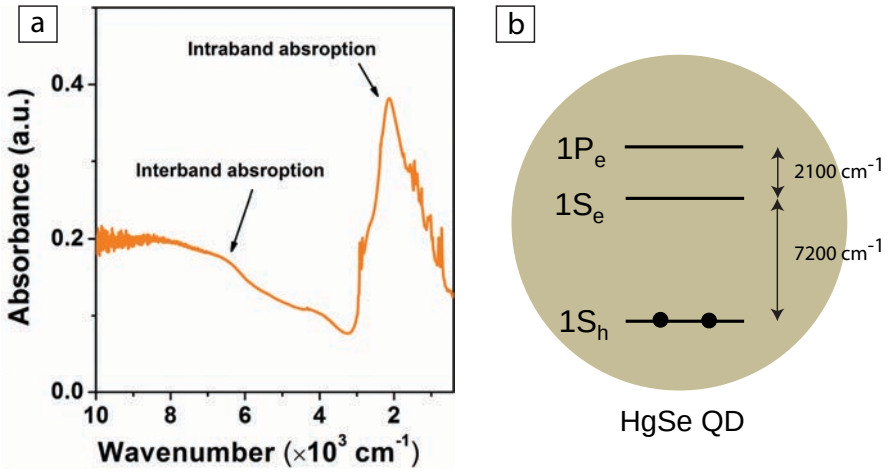

Figure 5.2: (a) Optical absorption spectrum of HgSe QDs. (b) The schematic of the intra-band gap is 2100 cm^{-1}, the inter-band gap is 7200 cm^{-1}.

gap, $\sim$ 0.2 eV. These values are consistent with the values obtained from optical absorption experiment.

The evolution of the spectrum as the gap voltage is changed depends on the carrier filling of the QD. At large negative voltage, regime I, the Fermi level is within the band gap as sketch figure 5.4 a. Consequently, the large inter-band gap is observed in the conductance spectrum. At lower gate voltage, regime II and regime III, the Fermi level is located on the first excited level $1S_e$. In the regime II, only a single electron is present on the $1S_e$ level. In regime III, two electrons are present on this level. Indeed, this level has a two-fold degeneracy because of the spin. The amplitude of the gap reaches a minimum at the charge degeneracy point between the regime II and regime III, figure 5.4 c. At this degeneracy point, the gap is controlled by the Coulomb energy and the spectrum has the characteristic look of a Coulomb diamond tip. At higher gate voltage,

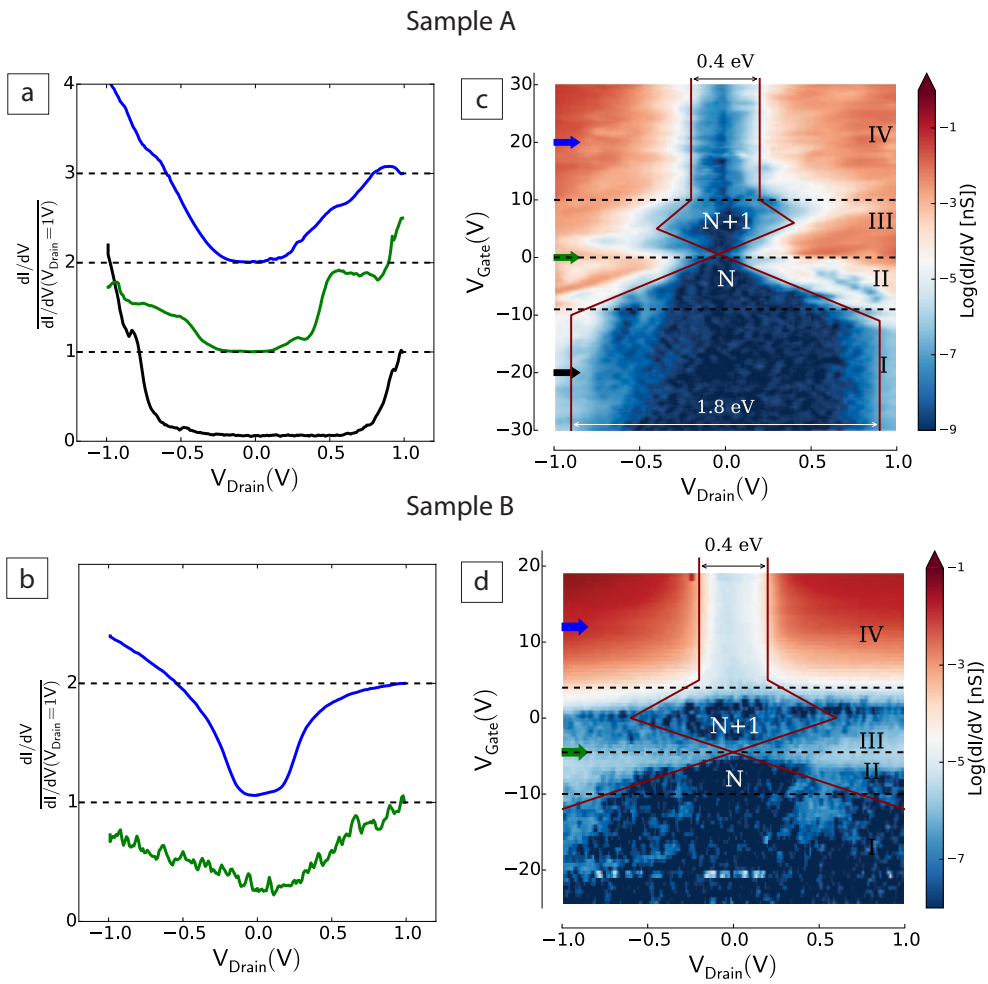

Figure 5.3: Conductance spectrum dI/dV as function of drain voltage and gate voltage measured on two samples A and B. The curves shown on panels (a) and (b) are extracted from the color maps (c) and (d), respectively, at the gate voltages indicated by the arrows. On the color plot, the dashed lines separate the different regimes labeled I to IV discussed in the text. The red lines indicate the edges of the main structures in the spectrum, i.e. gap edges and Coulomb edges.

regime IV, the Fermi level is within the intra-band gap, figure 5.4 d, consequently, this gap is observed in the conductance spectrum.

The novelty of the observed spectrum should be emphasized. Indeed, as dis-

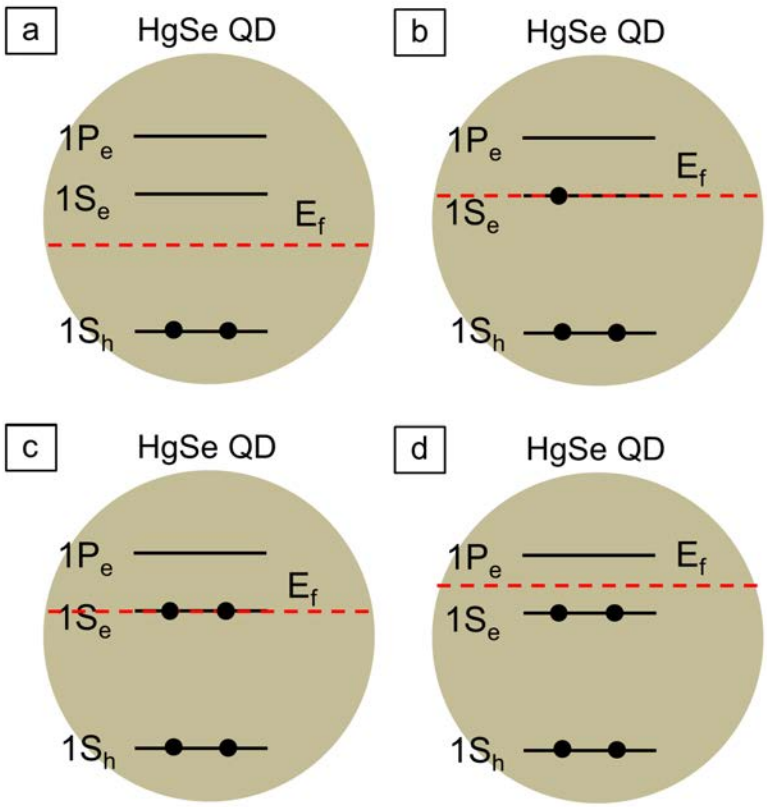

Figure 5.4: The schematic of the location of Fermi level in the HgSe QD at different gate voltages. The location of fermi level in (a), (b), (c) and (d) correspond to the gate voltages in regime I, II, III and IV in figure 5.3. The Fermi level is represented by the red dashed line.

cussed in chapter 2, most observations of discrete electronic spectrum have been done in large semiconducting QDs, where the density of states in the conduction band is large. Consequently, a metallic diamond structure is usually observed when the Fermi level is located within the conduction band. In contrast, in QDs, as the density of states is low even in the conduction band, with only a few levels $1S_e$, $1P_e$, etc, only n-1 Coulomb diamonds are present, where n is the degeneracy of the level. When the Fermi level is on the $1S_e$ level, the differential conductance

map shows a single Coulomb diamond, as observed in the spectra shown in figure 5.3. This is the first time that this type of electronic spectrum has been observed.

5.2 Photocurrent measurement on a single HgSe QD

Beyond its fundamental interest, the fabrication of single nanoparticle devices could be of interest for applications where single spins or single charges have to be manipulated. For example, the development of methods for reading the resonance frequency of single spins is of interest for application in quantum information[9] as well as for the development of chemical sensors. Among different methods currently developed for reading single spin states, one method has particularly attracted our attention[10]. This method is based on measurements of the photo current in P-doped silicon. It has been shown by Maxwell and Honig[11] and Schmidt and Solomon[12] that the photo-current depends on the spin polarization of trap centers. This phenomena allows the Electrical Detection of Magnetic Resonance (EDMR) through measurement of the photocurrent.

To progress in that direction, we attempted a measure of the photo-current across a single QD. To that end, we developed a method, described in chapter 3, where the drain bias is modulated at the frequency $\omega_0 = 17$ Hz and the power of the illuminating light is also modulated at the frequency $\omega_1 = 52$ Hz. Consequently, the resulting photocurrent is modulated at the frequency $\omega_0 + \omega_1 = 69$ Hz. A lock-in technique is employed to detect the signal at this frequency. The light is applied with a photo-diode (wavelength = 660 nm). The maximum

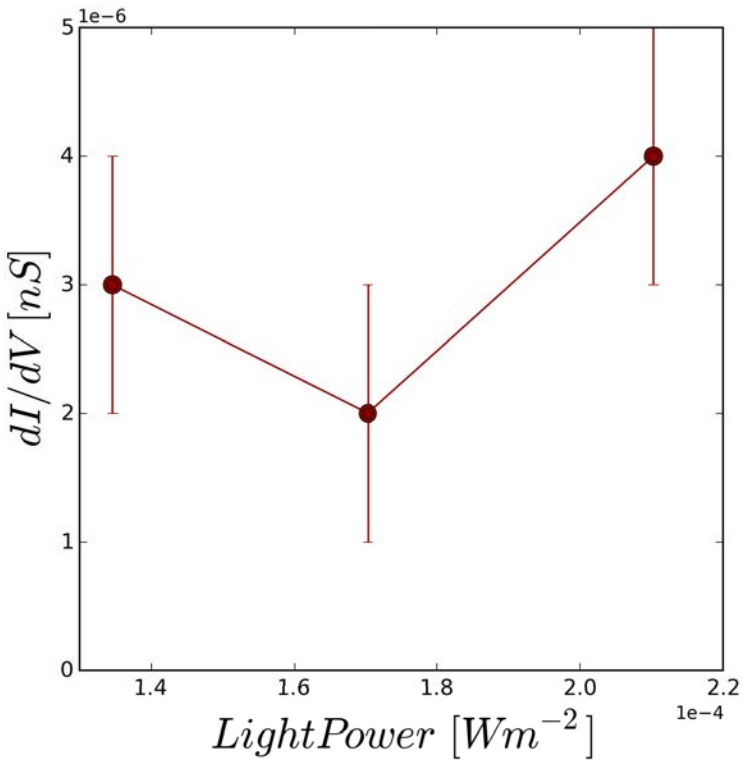

Figure 5.5: Photo-conductance dI/dV as function of light power of the LED diode.

light power applied is estimated to be about 2×10^{-4} Wm^{-2}. Measuring the photoconductance, at $V_{Drain} = 1$ V, at different LED power, we found that the photocurrent was quickly saturing at its maximum value and that no significant changes in the photocurrent was observed by doubling the LED power, as shown figure 5.5.

The major advantage of this method is to allow extracting the small photocurrent contribution, measured at the frequency $\omega_0 + \omega_1$, from the large direct tunnel current across the QDs measured at the frequency ω_0.

Figure 5.6 a and figure 5.6 b show, respectively, the conductance and the photoductance maps measured on sample A. A small photoconductance signal

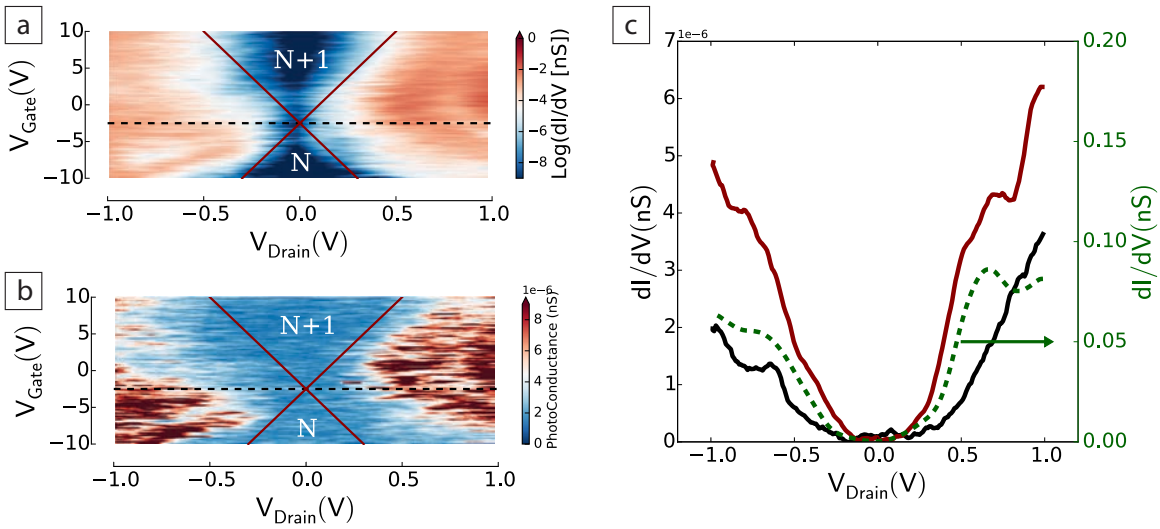

Figure 5.6: (a) Conductance spectrum measured under light illumination at the frequency ω_0, as function of drain and gate voltage. (b) Photo-conductance measured at the frequency $\omega_0 + \omega_1$, as function of drain and gate voltage. (c) The red line shows the photoconductance extracted from panel (b) compared with the dark conductance (black line). The dash line is the conductance spectrum extracted from panel (a).

can be clearly resolved. Figure 5.6 c shows the photoconductance as function of drain voltage compared with the conductance signal. While the direct tunnel conductance is about 0.1 nS at $V_{Drain} = 1$ V, the photoconductance is only 5×10^{-6} nS. While this signal is very small, it is clearly related to the light generated current. Indeed, measuring the photo-conductance while darkening the LED light, shows a strong reduction in the measured photocurrent by a factor of 2, well beyond experimental resolution.

As shown figure 5.5, the measured photocurrent quickly reached a maximum with the light power, indicating the absorption saturation of the QD. Assuming that only a single exciton can be created in the QD upon absorption of a pho-

ton, then the photocurrent will be limited by the lifetime τ of the exciton in the QD. Further, assuming that every exciton dissociates and contributes to the photocurrent, the maxium photo-current is related to the life time through the simple formula $I = 2e/\tau$. From the data, we extract a photocurrent $I_{PC} \sim 5 \times 10^{-6}$ nA at the drain voltage $V_{Drain} = 1$ V. This implies that the residence time of the exciton in the QD is equal to $\tau = 2e/I_{PC} \sim 65\ \mu s$. In QDs, the fluorescence lifetime is usually much lower than $1\mu s$ in the case of a direct recombination. However, in presence of an electron trap, the recombination between the electron and the hole can be much longer and fluorescence lifetime larger than 1 μs are commonly observed. Thus, it seems plausible that the residence time of the exciton could be as large as 65 μs before its dissociation and collection by the electrodes.

5.3 Conclusion

In this study of HgSe QDs, we studied the tunneling spectrum as function of electron occupation number. Upon increasing the carrier filling, the ETS shows the inter-band gap for the empty QD, a Coulomb blockade feature when the Fermi level is located on the two-fold degenerated first excited level $1S_e$, and finally, the intra-band gap when the Fermi level is located between the first and second excited levels. An additional remark on the band structure is in order. As described earlier, HgSe has an inverted band structure in the bulk. In theory, the band inversion should lead to the formation of surface states. We note that the interpretation of the experimental tunneling spectrum in our HgSe QDs did not require to take into account the possibility of surface states. This absence may indicate that the band structure should have recovered the normal order, i.e. with the Γ_6 band above the Γ_8 band, as expected in strongly confined QDs structures. A study as function of QD diameter would be of interest to identify the signature of surface states in the tunneling spectrum.

On this same system, we also attempted the first measurement of the photocurrent in a single colloidal QD. Recently, new developments in QDs synthesis allowed the preparation of QD doped with only a few doping atoms[13]. The fabrication of junctions with those doped QDs followed by measurements of the photocurrent provides a possible way for the electrical reading of a single spin.

Chapter 6

Conclusions and prospects

The goal of this thesis was to fabricate single nanoparticle junctions from colloidal solutions of semiconducting QDs. and study the electron tunneling spectroscopy of these junctions at low temperature. To overcome the difficulty of fabricating single nanoparticle junctions, we developed a method based on the projection in-vacuum of the nanoparticles onto the chip circuit. A first projection method, employing a fast pulsed valve, has been employed to fabricate single PbS QD junctions. To improve this projection system, I developed another setup based on the electrospray technique. The electrospray ionization system has been used to fabricate single HgSe QD junctions. All of the junctions are measured at low temperature, using a cryostat installed in a glove box under argon.

For PbS QD junctions, we found that the elastic and inelastic ETS of PbS QDs is characterized by signatures of strong electron-phonon coupling. In the shell-tunneling regime, the phonon modes can be observed in the *inelastic* ETS d^2I/dV^2. In the shell-filling regime, where the Coulomb blockade peaks are observed, the lowest energy phonon mode leads to the apparition of sub-bands that

can be observed in the *elastic* ETS dI/dV. In addition, in this regime, we found that the Coulomb blockade cannot be lifted at any gate voltage, which is likely the consequence of FC blockade. Thus, this first report of the observation of FC blockade induced by coupling of electrons to optical phonons teaches us that using QDs with weak electron-phonon coupling should help improve electronic transport in QDs thin films.

For the study of HgSe QD junctions, we observed the evolution of the tunneling spectrum as the QD occupation level is changed by gating. Upon increasing the carrier filling, the ETS shows either the inter-band gap for the empty QD, a Coulomb blockade feature when the Fermi level is located on the two-fold degenerated first excited level $1S_e$, and finally, the intra-band gap when the Fermi level is located between the first and second excited levels, $1S_e$ and $1P_e$. We note that the interpretation of this electronic spectrum did not require to take into account the possibility of surface states, indicating that the band structure should have recovered the normal order, i.e. with the Γ_6 above the Γ_8 band, as expected in strongly confined QDs structures. Furthermore, we attempted the first measure of the photocurrent across a single colloidal QD.

Regarding future works, a first proposal could be the study of the evolution of the band structure in HgSe QDs as function of their size. Indeed, as bulk HgSe has an inverted band but not the strongly confined QD, a study as function of QD diameter may allow the identification of the band crossing and possibly the formation of the surface states in the larger sized QDs. This study could be of much interest for the contemporary quest of topological materials.

Another possible direction of research would be to control more precisely the nanoparticle beam position. Indeed, as discussed earlier, the landing position

of the nanoparticles can be controlled by applying an electric field on the path followed by the beam. We can imagine that by precisely controlling the beam position, it could be possible to depose ordered arrays of nanoparticles.

Finally, another direction of research would be to employ doped QDs. Recently, new developments in QDs synthesis allowed the preparation of QD doped with only a few doping atoms. The fabrication of junctions with those doped QDs followed by measurements of the photocurrent provides a possible way for the electrical detection of the resonance of a single spin.

Chapter 7

Publications

[1] H. Wang, E. Lhuillier, Q. Yu, A. Mottaghizadeh, C. Ulysse, A. Zimmers, A. Descamps-Mandine, B. Dubertret & H. Aubin (2015). Tunneling spectroscopy and photocurrent measurement in a single HgSe QDot. *In preparation*.

[2] H. Wang, E. Lhuillier, Q. Yu, A. Mottaghizadeh, C. Ulysse, A. Zimmers, A. Descamps-Mandine, B. Dubertret & H. Aubin (2015). Effects of electron-phonon interactions on the electron tunneling spectrum of PbS quantum dots. *Physical Review B*, **92**, 041403(R).

[3] Q. Yu, A. Mottaghizadeh, H. Wang, C. Ulysse, A. Zimmers, V. Rebuttini, N. Pinna & H. Aubin (2014). Verwey transition in single magnetite nanoparticles. *Physical Review B*, **90**, 075122.

References

Chapter 1

[1] J. C. Hulteen, H. X. Chen, C. K. Chambliss, and C. R. Martin, Reports on Progress in Physics **64**, 297 (2001).

[2] D. V. Talapin, J.-S. Lee, M. V. Kovalenko, and E. V. Shevchenko, Chemical reviews **110**, 389 (2010), doi.

[3] A. P. Alivisatos, Science **271**, 933 (1996), doi.

[4] T. S. Nanocrystallites, C. B. Murray, D. J. Noms, and M. G. Bawendi, Journal of the American Chemical socie **115**, 8706 (1993).

[5] M. S. Gudiksen and C. M. Lieber, Journal of the American Chemical Society **122**, 8801 (2000), doi.

[6] S. Kudera *et al.*, Nano Letters **5**, 445 (2005), doi.

[7] M. D. Tessier *et al.*, Nano Letters **14**, 207 (2014), doi.

[8] B. Mahler, B. Nadal, C. Bouet, G. Patriarche, and B. Dubertret, Journal of the American Chemical Society **134**, 18591 (2012), doi.

[9] S. Ithurria *et al.*, Nature materials **10**, 936 (2011), doi.

[10] A. D. Stiff-Roberts, K. R. Lantz, and R. Pate, Journal of Physics D: Applied Physics **42**, 234004 (2009), doi.

[11] P. Zrazhevskiy, M. Sena, and X. Gao, Chemical Society reviews **39**, 4326 (2010), eprint, doi.

[12] C. Kittel, *Introduction to solid state physics*, 8th ed. (Wiley, 2005).

[13] A. L. Rogach, A. Eychmüller, S. G. Hickey, and S. V. Kershaw, Small **3**, 536 (2007), doi.

[14] E. P. A. M. Bakkers *et al.*, Nano Letters **1**, 551 (2001), doi.

[15] O. Millo, D. Katz, Y. Cao, and U. Banin, Physical Review Letters **86**, 5751 (2001), doi.

[16] U. Banin, Y. Cao, D. Katz, and O. Millo, Nature **400**, 542 (1999), doi.

[17] B. Diaconescu, L. a. Padilha, P. Nagpal, B. S. Swartzentruber, and V. I. Klimov, Physical Review Letters **110**, 127406 (2013), doi.

[18] G. A. Grinbom *et al.*, Physical Review B **81**, 245301 (2010), doi.

[19] K. Overgaag, P. Liljeroth, B. Grandidier, and D. Vanmaekelbergh, ACS Nano **2**, 600 (2008), doi.

[20] Q. Yu *et al.*, ACS nano **7**, 1487 (2013), doi.

[21] Q. Yu *et al.*, Physical Review B **90**, 75122 (2014), doi.

[22] H. Wang *et al.*, Physical Review B **92**, 041403 (2015), doi.

Chapter 2

[1] M. Buttiker, Y. Imry, R. Landauer, and S. Pinhas, Physical Review B **31**, 6207 (1985), doi.

[2] R. Landauer, Philosophical Magazine **21**, 863 (1970), doi.

[3] J. G. Simmons, Journal of Applied Physics **34**, 1793 (1963), doi.

[4] L. P. Kouwenhoven, D. G. Austing, and S. Tarucha, Reports on Progress in Physics **64**, 701 (2001).

[5] E. P. A. M. Bakkers *et al.*, Nano Letters **1**, 551 (2001), doi.

[6] O. Millo, D. Katz, Y. Cao, and U. Banin, Physical Review Letters **86**, 5751 (2001), doi.

[7] U. Banin, Y. Cao, D. Katz, and O. Millo, Nature **400**, 542 (1999), doi.

[8] B. Diaconescu, L. a. Padilha, P. Nagpal, B. S. Swartzentruber, and V. I. Klimov, Physical Review Letters **110**, 127406 (2013), doi.

[9] G. A. Grinbom *et al.*, Physical Review B **81**, 245301 (2010), doi.

[10] K. Overgaag, P. Liljeroth, B. Grandidier, and D. Vanmaekelbergh, ACS Nano **2**, 600 (2008), doi.

[11] P. Liljeroth *et al.*, Physical Review Letters **95**, 086801 (2005), doi.

[12] F. Kuemmeth, K. I. Bolotin, S.-F. Shi, and D. C. Ralph, Nano letters **8**, 4506 (2008), doi.

[13] Q. Yu *et al.*, Physical Review B **90**, 75122 (2014), doi.

[14] D. L. Klein, R. Richard, K. L. Andrew, a. P. Alivisatos, and P. L. Mceuen, Nature **389**, 699 (1997), doi.

[15] P. Yu and M. Cardona*Fundamentals of semiconductors: physics and materials properties* Vol. 1, 4th ed. (Springer, 2005), doi.

[16] J. C. Hulteen, H. X. Chen, C. K. Chambliss, and C. R. Martin, Reports on Progress in Physics **64**, 297 (2001).

[17] C. Kittel, *Introduction to solid state physics*, 8th ed. (Wiley, 2005).

[18] A. P. Alivisatos, Science **271**, 933 (1996), doi.

[19] J. W. Luo, A. Franceschetti, and A. Zunger, Nano Letters **8**, 3174 (2008), doi.

[20] U. Elfurawi, *Optical and Electronic Properties of PbS Colloidal Nanocrystals*, PhD thesis, University of Nottingham, (2012).

[21] J. J. Urban, D. V. Talapin, E. V. Shevchenko, C. R. Kagan, and C. B. Murray, Nature materials **6**, 115 (2007), doi.

[22] D. V. Talapin and C. B. Murray, Science (New York, N.Y.) **310**, 86 (2005), doi.

[23] O. Madelung, *Semiconductors*, 3th ed. (Springer, 2004).

[24] E. Lhuillier, A. Robin, S. Ithurria, H. Aubin, and B. Dubertret, Nano letters **14**, 2715 (2014), doi.

[25] G. Konstantatos *et al.*, Nature **442**, 180 (2006), doi.

[26] A. Pandey and P. Guyot-Sionnest, Science (New York, N.Y.) **322**, 929 (2008), doi.

[27] Z. Chen, B. Nadal, B. Mahler, H. Aubin, and B. Dubertret, Advanced Functional Materials **24**, 295 (2014), doi.

[28] M. Rohlfing and S. Louie, Physical Review B **57**, R9392 (1998), doi.

[29] a. Delin and T. Klüner, Physical Review B **66**, 035117 (2002), doi.

[30] K. U. Gawlik, L. Kipp, M. Skibowski, N. Orlowski, and R. Manzke, Physical Review Letters **78**, 3165 (1997), doi.

[31] D. Eich *et al.*, Physical Review B **61**, 12666 (2000), doi.

[32] B. Yan and S.-C. Zhang, Reports on Progress in Physics **75**, 096501 (2012), doi.

[33] a. Svane *et al.*, Physical Review B - Condensed Matter and Materials Physics **84**, 205205 (2011), doi.

[34] R. Leturcq *et al.*, Nature Physics **5**, 327 (2009), doi.

[35] D. V. Talapin, J.-S. Lee, M. V. Kovalenko, and E. V. Shevchenko, Chemical reviews **110**, 389 (2010), doi.

[36] Z. Sun, I. Swart, C. Delerue, D. Vanmaekelbergh, and P. Liljeroth, Physical Review Letters **102**, 196401 (2009), doi.

[37] Q. Yu *et al.*, ACS nano **7**, 1487 (2013), doi.

Chapter 3

[1] A. Nag *et al.*, Journal of the American Chemical Society **133**, 10612 (2011), doi.

[2] E. Lhuillier, A. Robin, S. Ithurria, H. Aubin, and B. Dubertret, Nano letters **14**, 2715 (2014), doi.

[3] Q. Yu *et al.*, ACS nano **7**, 1487 (2013), doi.

[4] Q. Yu *et al.*, Physical Review B **90**, 75122 (2014), doi.

[5] H. Wang *et al.*, Physical Review B **92**, 041403 (2015), doi.

[6] J. B. Fenn, M. Mann, C. K. Meng, S. F. Wong, and C. M. Whitehouse, Science **246**, 64 (1989), doi.

[7] J. B. Fenn, M. Mann, C. K. Meng, S. F. Wong, and C. M. Whitehouse, Mass Spectrometry Reviews **9**, 37 (1990), doi.

[8] P. Kebarle and L. Tang, Analytical Chemistry **65**, 972A (1993), doi.

[9] A. P. Bruins, Journal of Chromatography A **794**, 345 (1998), doi.

[10] C. S. Ho *et al.*, The Clinical biochemist. Reviews / Australian Association of Clinical Biochemists **24**, 3 (2003).

[11] S. Rauschenbach *et al.*, Small **2**, 540 (2006), doi.

[12] A. Saywell *et al.*, Angewandte Chemie - International Edition **49**, 9136 (2010), doi.

[13] D. V. Kondratuk *et al.*, Angewandte Chemie - International Edition **51**, 6696 (2012), doi.

[14] M. Weston, A. J. Britton, and J. N. O'Shea, Journal of Chemical Physics **134**, 054705 (2011), doi.

[15] M. C. O'Sullivan *et al.*, Nature **469**, 72 (2011), doi.

[16] A. J. Britton *et al.*, Journal of Chemical Physics **135**, 164702 (2011), doi.

[17] J. N. O'Shea *et al.*, Nanotechnology **18**, 035707 (2007), doi.

[18] C. J. Satterley *et al.*, Nanotechnology **18**, 455304 (2007), doi.

[19] A. Saywell *et al.*, Journal of Physical Chemistry C **112**, 7706 (2008), doi.

[20] A. Saywell *et al.*, Nature communications **1**, 75 (2010), doi.

[21] M. Weston, K. Handrup, T. J. Reade, N. R. Champness, and J. N. O'Shea, The Journal of chemical physics **137**, 224706 (2012), doi.

[22] L. C. Mayor *et al.*, Journal of Chemical Physics **129**, 114701 (2008), doi.

[23] L. C. Mayor *et al.*, Journal of Chemical Physics **130**, 164704 (2009), doi.

[24] A. Saywell *et al.*, Nanotechnology **22**, 075704 (2011), doi.

[25] M. Weston *et al.*, Journal of Chemical Physics **135**, 114703 (2011), doi.

[26] K. Handrup, V. J. Richards, M. Weston, N. R. Champness, and J. N. O'Shea, Journal of Chemical Physics **139**, 154708 (2013), doi.

Chapter 4

[1] Z. Chen, B. Nadal, B. Mahler, H. Aubin, and B. Dubertret, Advanced Functional Materials **24**, 295 (2014), doi.

[2] R. D. Schaller and V. I. Klimov, Physical Review Letters **92**, 186601 (2004), eprint, doi.

[3] D. V. Talapin and C. B. Murray, Science (New York, N.Y.) **310**, 86 (2005), doi.

[4] Q. Yu *et al.*, Physical Review B **90**, 75122 (2014), doi.

[5] Q. Yu *et al.*, ACS nano **7**, 1487 (2013), doi.

[6] U. Banin and O. Millo, Annual review of physical chemistry **54**, 465 (2003), doi.

[7] L. Jdira *et al.*, Physical Review B **77**, 1 (2008), doi.

[8] Z. Sun, I. Swart, C. Delerue, D. Vanmaekelbergh, and P. Liljeroth, Physical Review Letters **102**, 196401 (2009), doi.

[9] B. Diaconescu, L. a. Padilha, P. Nagpal, B. S. Swartzentruber, and V. I. Klimov, Physical Review Letters **110**, 127406 (2013), doi.

[10] I. Kang and F. W. Wise, Journal of the Optical Society of America B **14**, 1632 (1997), doi.

[11] P. Liljeroth *et al.*, Physical Review Letters **95**, 086801 (2005), doi.

[12] G. A. Grinbom *et al.*, Physical Review B **81**, 245301 (2010), doi.

[13] Y. Niquet, C. Delerue, G. Allan, and M. Lannoo, Physical Review B **65**, 165334 (2002), doi.

[14] L. P. Kouwenhoven, D. G. Austing, and S. Tarucha, Reports on Progress in Physics **64**, 701 (2001), doi.

[15] T. H. Nguyen *et al.*, Physical Review B **84**, 1 (2011), doi.

[16] N. S. Wingreen and J. W. Wilkins, Physical Review B **40**, 11834 (1989), doi.

[17] A. Mitra, I. Aleiner, and A. J. Millis, Physical Review B **69**, 245302 (2004), doi.

[18] C. Delerue and M. Lannoo, *Nanostructures: Theory and Modelling* (Springer, 2004), web.

[19] J. Park *et al.*, Nature **407**, 57 (2000), doi.

[20] R. H. M. Smit *et al.*, Nature **419**, 906 (2002), doi.

[21] X. H. Qiu, G. V. Nazin, and W. Ho, Physical Review Letters **92**, 206102 (2004), doi.

[22] S. Sapmaz, P. Jarillo-Herrero, Y. Blanter, C. Dekker, and H. van der Zant, Physical Review Letters **96**, 26801 (2006), doi.

[23] R. Leturcq *et al.*, Nature Physics **5**, 327 (2009), doi.

[24] T. Krauss, F. Wise, and D. Tanner, Physical review letters **76**, 1376 (1996), web.

[25] T. D. Krauss and F. W. Wise, Physical Review B **55**, 9860 (1997), doi.

[26] T. Krauss and F. Wise, Physical Review Letters **79**, 5102 (1997), doi.

[27] J. Bylsma *et al.*, Physical Review B **86**, 125322 (2012), doi.

[28] J. Koch and F. von Oppen, Physical Review Letters **94**, 206804 (2005), doi.

[29] J. Koch, F. von Oppen, and a. Andreev, Physical Review B **74**, 205438 (2006), doi.

[30] D. Sagar *et al.*, Physical Review B **77**, 235321 (2008), doi.

[31] O. Verzelen, R. Ferreira, and G. Bastard, Phys. Rev. Lett. **88**, 146803 (2002), doi.

[32] P. K. Hansma*Tunneling Spectroscopy: Capabilities, Applications, and New Techniques* Vol. 9 (Plenum Press, 1982), web.

[33] P. Nagpal and V. I. Klimov, Nature communications **2**, 486 (2011), doi.

Chapter 5

[1] X. W. Zhang and J. B. Xia, Journal of Physics D: Applied Physics **39**, 1815 (2006), doi.

[2] H. Mirzai *et al.*, Journal of Materials Chemistry C **2**, 2107 (2014), doi.

[3] Z. Deng, K. S. Jeong, and P. Guyot-sionnest, ACS Nano **8**, 11707 (2014).

[4] M. K. Jana *et al.*, Journal of Materials Chemistry C **1**, 6184 (2013), doi.

[5] S. Keuleyan, E. Lhuillier, V. Brajuskovic, and P. Guyot-Sionnest, Nature Photonics **5**, 489 (2011), doi.

[6] E. Lhuillier, S. Keuleyan, and P. Guyot-Sionnest, Nanotechnology **23**, 175705 (2012), doi.

[7] E. Lhuillier, S. Keuleyan, H. Liu, and P. Guyot-Sionnest, Chemistry of Materials **25**, 1272 (2013), doi.

[8] E. Lhuillier *et al.*, In preparation (2015).

[9] I. Buluta, S. Ashhab, and F. Nori, Reports on Progress in Physics **74**, 104401 (2011), doi.

[10] A. R. Stegner *et al.*, Nature Physics **2**, 835 (2006), doi.

[11] R. Maxwell and A. Honig, Physical Review Letters **17**, 188 (1966), doi.

[12] S. I. Schmidt J, Compte Rendue de l'académie des sciences Série B **263**, 72 (1966).

[13] D. J. Norris, A. L. Efros, and S. C. Erwin, Science (New York, N.Y.) **319**, 1776 (2008), doi.